

---

# Multimodal Crystal Flow: Any-to-Any Modality Generation for Unified Crystal Modeling

---

Kiyoung Seong<sup>1,2</sup> Sungsoo Ahn<sup>1</sup> Sehui Han<sup>2</sup> Changyoung Park<sup>2</sup>

## Abstract

Crystal modeling spans a family of conditional and unconditional generation tasks across different modalities, including crystal structure prediction (CSP) and *de novo* generation (DNG). While recent deep generative models have shown promising performance, they remain largely task-specific, lacking a unified framework that shares crystal representations across different generation tasks. To address this limitation, we propose *Multimodal Crystal Flow (MCFlow)*, a unified multimodal flow model that realizes multiple crystal generation tasks as distinct inference trajectories via independent time variables for atom types and crystal structures. To enable multimodal flow in a standard transformer model, we introduce a composition- and symmetry-aware atom ordering with hierarchical permutation augmentation, injecting strong compositional and crystallographic priors without explicit structural templates. Experiments on the MP-20 and MPTS-52 benchmarks show that MCFlow achieves competitive performance against task-specific baselines across multiple crystal generation tasks.

## 1. Introduction

Crystal discovery based on atomic structures is vital for developing next-generation functional materials such as battery electrolytes and catalysts (Butler et al., 2018). However, traditional approaches are computationally prohibitive due to expensive density functional theory (DFT) calculations (Glass et al., 2006; Wang et al., 2010; Pickard & Needs, 2011; Wang et al., 2012). To address this issue, prior work has introduced generative models that learn distributions of stable crystals from data under various conditional or unconditional generation schemes, each corresponding to a distinct crystal generation setting (Xie & Grossman, 2018;

Nouira et al., 2018; Hoffmann et al., 2019; Noh et al., 2019; Court et al., 2020; Dan et al., 2020; Ren et al., 2020; Kim et al., 2020; Zhao et al., 2021; Long et al., 2021; Zhao et al., 2023; Nguyen et al., 2023; Tangsongcharoen et al., 2025; Cao et al., 2025). Recent methods have incorporated crystallographic symmetry within specific generation settings via structural templates (Zhu et al., 2024; Jiao et al., 2024).

At a high level, crystal modeling spans a family of generation problems across different modalities. Depending on which modalities are observed, this formulation naturally covers crystal structure prediction (CSP), *de novo* generation (DNG), and structure-conditioned atom type generation. This perspective aligns with a broader trend in generative modeling toward unified frameworks where a single model supports multiple conditional generation tasks across modalities (Campbell et al., 2024; Rojas et al., 2025). However, existing crystal generative models adopt task-specific formulations, necessitating separate training for different generation settings and hindering a unified formulation that reuses the same underlying crystal representations across tasks.

In this work, we introduce *Multimodal Crystal Flow (MCFlow)*, a unified generative model that enables any-to-any modality generation across atom types and crystal structures (Figure 1). The key insight is that by decoupling flow time axes for different modalities, a single model can flexibly condition on any subset of modalities while generating the rest, without retraining or task-specific architectures. This design allows a single MCFlow model to support CSP, DNG, and atom type generation.

We instantiate MCFlow using a diffusion transformer (DiT) architecture (Peebles & Xie, 2023), following recent successes in all-atom molecular and crystalline modeling (Joshi et al., 2025; Frank et al., 2025; Yi et al., 2025). However, the DiT lacks inductive biases for crystallographic symmetry and permutation invariance. To address this, we introduce a composition- and symmetry-aware atom ordering and hierarchical permutation augmentation. By lexicographically sorting atoms based on electronegativity and Wyckoff positions, we enable the DiT to internalize chemical and crystallographic structure from data without relying on explicit structural templates. The hierarchical permutation augmentation then enforces invariance across and within symmetry-

<sup>1</sup>Department of AI, KAIST, Seoul, South Korea <sup>2</sup>Materials Intelligence Lab, LG AI Research, Seoul, South Korea. Correspondence to: Changyoung Park <changyoung.park@lgresearch.ai>.

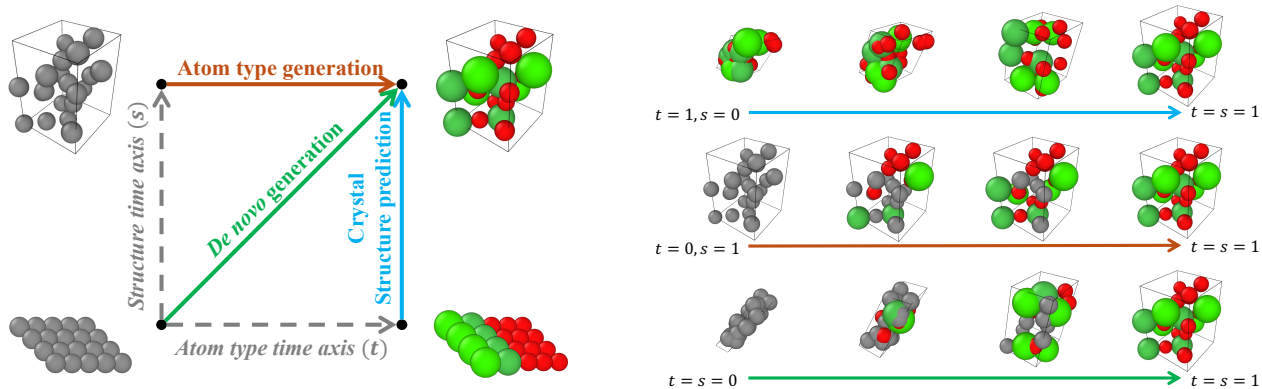


Figure 1. **Overview of multimodal crystal flow with any-to-any modality generation.** MCFlow trains a flow model with two independent time variables corresponding to atom types ( $t$ ) and structures ( $s$ ). By selecting task-specific inference trajectories in the  $(t, s)$  space, a single model performs crystal structure prediction, atom type generation, and *de novo* generation.

equivalent orbits, providing a structured inductive bias over compositionally and crystallographically equivalent atoms.

Our main contributions are as follows:

- We introduce *MCFlow*, a unified multimodal flow framework for crystal generation that enables any-to-any modality generation across atom types and crystal structures within a single model.
- We propose a composition- and symmetry-aware atom ordering strategy that enables DiT architectures to encode composition and crystallographic symmetry priors without explicit symmetry constraints.
- We introduce hierarchical inter- and intra-orbit permutation augmentation over symmetry-equivalent atoms, promoting permutation robustness.
- We demonstrate that *MCFlow*, together with the proposed ordering and augmentation strategies, achieves competitive performance in crystal structure prediction, *de novo* generation, and structure-conditioned atom type generation using a single model.

## 2. Related Work

**Crystal generative models.** Recent advances in diffusion- and flow-based generative models have significantly improved the fidelity and stability of generated crystal structures. Diffusion models (Xie et al., 2021; Jiao et al., 2023; Yang et al., 2023; Zeni et al., 2023) model crystal generation as iterative denoising of atomic coordinates in a primitive unit cell. More recent work has explored flow-based models and stochastic interpolants (Miller et al., 2024; Sriram et al., 2024; Luo et al., 2025; Hoellmer et al., 2025). ADiT (Joshi et al., 2025) adopts latent diffusion frameworks with diffusion transformer architecture for all-atom molecular and

crystalline modeling. However, these models generally lack explicit inductive biases for crystallographic symmetry.

Alternative approaches enforce symmetry by generating structural templates (Kazeev et al., 2024; Zhu et al., 2024; Kelvinius et al., 2025) or restricting generation to the asymmetric unit (ASU) (Jiao et al., 2024; Levy et al., 2025; Chang et al., 2025; Puny et al., 2025) conditioned on structural templates. While these methods satisfy crystallographic constraints, they are tailored to specific conditional generation settings and often rely on task-dependent structural template generation or retrieval modules. In contrast, *MCFlow* supports unified modeling of CSP, DNG, and atom type generation within a single end-to-end model by incorporating crystallographic symmetry as a soft inductive bias without structural template modules.

**Any-to-any multimodal generative models.** Recent diffusion- and flow-based generative frameworks increasingly adopt unified multimodal formulations to jointly model heterogeneous modalities. By decoupling modality-wise time axes, these frameworks enable flexible conditional generation, including any-to-any settings. *Multiflow* (Campbell et al., 2024) applies this paradigm to jointly model amino acid sequences and structures for protein co-design, while Rojas et al. (2025) generalize multimodal diffusion models to arbitrary state spaces with applications to text-image domains. Despite their success, extending such frameworks to crystalline materials remains nontrivial due to periodic boundary conditions and crystallographic symmetry. *MCFlow* extends this multimodal generative paradigm to periodic crystal systems by decoupling atom types and crystal structures with modality-wise time axes, enabling a unified framework that supports CSP, DNG, and atom type generation without task-specific architectures or retraining.

### 3. Method

In this section, we present a multimodal flow framework for unified crystal generation that supports flexible conditional generation across atom types and crystal structures within a single model. The core idea is to decouple the generative processes of different modalities through modality-specific time parameterization, allowing diverse crystal generation tasks to be realized within a shared model. Building on this formulation, we introduce a composition- and symmetry-aware atom ordering together with permutation augmentation, which provides a soft inductive bias for transformer-based architectures to robustly learn crystallographic symmetry and chemical composition. Notations and background on crystal representations and flow models on various state spaces are provided in Appendix A.

#### 3.1. Multimodal Flow Model for Crystals

Our goal is to generate arbitrary subsets of modalities while conditioning on the others. Standard diffusion or flow models rely on a single shared time variable, which couples all modalities to the same noise level and restricts conditional generation. We address this limitation by decoupling flow time variables to atom types and crystal structures and learning a joint generative process over a two-dimensional time space. Intuitively, this decoupling allows the model to hold one modality fixed while sampling the other, providing controllable conditional generation. Different crystal generation tasks can be realized through inference-time trajectory selection, as shown in Figure 1.

**Multimodal flow model.** We adopt a multimodal flow model with decoupled flow time variables  $t, s \in [0, 1]$  corresponding to atom types  $A \in \mathbb{Z}_+^N$  and crystal structures  $X = (F, L^l, L^a)$  in the primitive unit cell which consists of fractional coordinates  $F \in [0, 1]^{3 \times N}$ , Niggli-reduced lattice lengths  $L^l = (a, b, c) \in \mathbb{R}^{1 \times 3}$ , and angles  $L^a = (\alpha, \beta, \gamma) \in [60^\circ, 120^\circ]^{1 \times 3}$ . After training the flow model, we select an inference trajectory in a  $(t, s)$  time plane to realize different crystal discovery tasks with observed modalities fixed at 1. All tasks share identical flow model and require no task-specific models or retraining.

To describe the multimodal flow model, we first design the joint probability path  $p_{t,s}(A_t, X_s)$  defined by marginalizing modality-wise conditional paths:

$$p_{t,s}(A_t, X_s) = \int p_t(A_t | A_0, A_1) p_s(X_s | X_0, X_1) d\pi, \quad (1)$$

where  $\pi(A_0, X_0, A_1, X_1) = p_0(A_0, X_0)p_1(A_1, X_1)$  is the independent coupling between joint base  $p_0$  and data  $p_1$  distributions over atom types and structures.

This joint path evolves through a continuous-time Markov

chain (CTMC) over atom types along the  $t$ -axis and an ordinary differential equation (ODE) over crystal structures along the  $s$ -axis:

$$p_{t+h|t,s}(\cdot | A_t, X_s) = \delta_{A_t} + h u^A(A_t, X_s, t, s) + o(h), \quad (2)$$

$$\frac{dX_s}{ds} = u^X(A_t, X_s, t, s), \quad (3)$$

where  $u^A(A_t, X_s, t, s)$  denotes the rate vector of the CTMC over atom types in a discrete state space,  $u^X(A_t, X_s, t, s)$  denotes the velocity field of the ODE over crystal structures in a continuous state space, and  $o(h)$  denotes residual terms that vanish as  $h \rightarrow 0$ . The  $t$ -axis governs atom type updates conditioned on crystal structures, whereas the  $s$ -axis handles structure updates conditioned on atom types.

**Multimodal flow matching.** We adopt a flow matching objective to learn modality-specific vector fields or rate vectors for the decoupled generative processes. Our objective is to minimize a weighted sum of divergences between the model prediction and the target velocity field or rate vector for each modality:

$$\mathcal{L}(\theta) = \mathbb{E}_{t,s,A_t,X_s} \left[ \sum_{m \in \{A,X\}} w_m D_m(u_\theta^m, u^m) \right], \quad (4)$$

where  $u_{(\theta)}^m = u_{(\theta)}^m(A_t, X_s, t, s)$ ,  $D_A$  is generalized KL divergence for atom types and  $D_X$  is squared Euclidean distance for crystal structures.

For tractable supervision, we match to modality-wise conditional targets  $u^A(A_t | A_0, A_1)$  and  $u^X(X_s | X_0, X_1)$  rather than directly the marginal velocity field or rate vector, since they are the expectation of the modality-wise conditional targets through posterior coupling

$$u^A = \mathbb{E}_{A_0, A_1} [u^A(A_t | A_0, A_1) | A_t, X_s], \quad (5)$$

$$u^X = \mathbb{E}_{X_0, X_1} [u^X(X_s | X_0, X_1) | A_t, X_s]. \quad (6)$$

Under these divergences, the conditional flow matching objective induces the same gradient with respect to the model parameters as matching the marginal target implied by this posterior expectation (Lipman et al., 2024). We construct conditional target velocity fields or rate vector as follows: straight line flows between prior and target samples for lattice parameter, geodesic flows between prior and target samples on the torus manifold  $\mathbb{T}^{3 \times N}$  for fractional coordinates (Miller et al., 2024) to enforce periodicity, and mixture paths between two point masses of prior and target samples for atom types; full expressions are provided in Appendix B.

**Parameterization and base distributions.** We adopt clean data prediction across all modalities instead of predicting noise or velocity targets, motivated by the manifold structure

Index	Element	Wyckoff_position	Orbit_index	X	Y	Z
0	Th	a	0	0.0000	0.0000	0.0000
1	Th	c	1	0.6018	0.6018	0.1945
2	Th	c	1	0.3982	0.3982	0.8055
3	Th	c	2	0.2003	0.2003	0.3992
4	Th	c	2	0.7997	0.7997	0.6008
5	C	b	3	0.5000	0.5000	0.5000

Inter-orbit permutation (curved arrow from row 1 to row 3)

Intra-orbit permutation (curved arrows from row 1 to row 2 and from row 3 to row 4)

**Figure 2. Composition- and symmetry-aware atom ordering with hierarchical permutation augmentation.** Atoms in the primitive unit cell are lexicographically ordered by Pauling electronegativity and Wyckoff position (denoted by letter  $a, b, c, \dots$ ) to expose compositional and crystallographic structure. The ordering and augmentation are illustrated on a  $\text{Th}_5\text{C}$  crystal in the  $\text{R}\bar{3}\text{m}$  space group. Inter-orbit permutation reorders orbits sharing the same elements and Wyckoff position, while intra-orbit permutation permutes atoms within each orbit. This ordering and hierarchical permutation augmentation provides compositional and crystallographic symmetry information to sequence-based Transformers without explicitly conditioning space group or Wyckoff positions.

of data distribution (Li & He, 2025). For fractional coordinates, we predict fractional coordinates  $F_\theta$  and project them onto the torus  $\mathbb{T}^{3 \times N}$  via  $\text{proj}(F) = F \pmod{1}$ . We use a uniform base distribution on  $\mathbb{T}^{3 \times N}$  for fractional coordinates. For lattice length and angles, we predict directly  $L_\theta^l$  and  $L_\theta^a$ , using LogNormal priors for lengths to ensure positivity (Miller et al., 2024) and uniform priors for angles. For atom types, we predict atom type logits  $A_\theta$  with a mask-token point mass  $\delta_M$  as base distribution.

**Diffusion transformer.** For all-atom modeling of crystals, we adopt a Diffusion Transformer (DiT) backbone (Peebles & Xie, 2023) with modality-specific time conditioning and prediction heads tailored to the proposed multimodal flow. We embed all modalities with positional embeddings to obtain a token embedding as follows:

$$z = \text{Emb}(A) + \text{Lin}(F) + \text{Lin}(L^l) + \text{Lin}(L^a) + \text{PosEmb}, \quad (7)$$

where  $\text{Lin}(\cdot)$  denotes modality-specific linear layer and lattice embeddings are broadcasted to all atom tokens. The joint conditioning vector for learnable layer normalization is a sum of modality-wise time embeddings

$$c = \text{TimeEmb}(t) + \text{TimeEmb}(s), \quad (8)$$

where  $\text{TimeEmb}(\cdot)$  denotes modality-specific time embedding layer. We feed the multimodal embedding vector  $z$  and the conditioning vector  $c$  into the DiT backbone,  $h = \text{DiT}(z, c)$ . From the token-wise representations, we linearly predict atom type logits and fractional coordinates,

$$A_\theta = \text{Lin}(h), \quad F_\theta = \text{Lin}(h). \quad (9)$$

Global lattice parameters are predicted via mean pooling.

$$L_\theta^l = \text{Lin}(\bar{h}), \quad L_\theta^a = \text{Lin}(\bar{h}), \quad \bar{h} = \frac{1}{N} \sum_{i=1}^N h_i. \quad (10)$$

The final velocity field and rate vector are constructed from these outputs as provided in Appendix B. Since crystals

have variable numbers of atoms, we pad sequences within a batch and use attention masks; the pooling for lattice heads is computed over non-padded atom tokens only.

**Inference-time guidance.** To improve sample fidelity in our multimodal flow framework, we adopt noisy guidance (NG; Rojas et al., 2025), originally introduced for diffusion score models, and apply it to the velocity field of multimodal flow as an inference-time technique for conditional generation. This follows from the probability flow ODE formulation (Song et al., 2020), where the score function and the velocity field are deterministically related. For crystal structure prediction, the guided velocity field is given by

$$u_{\text{ng}}^X(A_1, X_s, 1, s) = (1 - \omega) u^X(A_\sigma, X_s, \sigma, s) + \omega u^X(A_1, X_s, 1, s). \quad (11)$$

where  $\sigma$  controls the corruption level of the conditioning modality and  $\omega$  denotes the guidance scale, biasing inference trajectories toward the regions favored by the conditional velocity field. The noisy guidance procedure is summarized in Algorithm 3, with additional ablation and sensitivity analyses provided in Appendix E.

### 3.2. Composition- and Symmetry-Aware Atom Ordering and Hierarchical Augmentation

This subsection introduces an atom ordering and augmentation strategy for the DiT architecture, designed to support multimodal flow models by explicitly incorporating compositional and crystallographic symmetry information.

Prior work has proposed ordering atoms in crystal structures according to their Wyckoff positions for an autoregressive transformer model, leveraging crystallographic symmetry (Cao et al., 2024). While effective, a direct application of such symmetry-based ordering to the DiT for multimodal flow model suffers from two limitations. First, in crystal structure prediction (CSP), where only the composition is given, the absence of structural symmetry information at inference time leads to ambiguity in defining the initial

atom ordering for the DiT. Second, this ordering does not explicitly encode chemical information, which can limit the model’s ability to learn compositionally valid crystals.

**Composition- and symmetry-aware atom ordering.** To address these limitations, we propose a lexicographical atom ordering that jointly incorporates compositional and crystallographic information. As illustrated in Figure 2, we first partition atoms into symmetry-equivalent groups  $O = \{g \cdot f \mid g \in G\}$  under the action of the space group  $G$ , referred to as *orbits*. Each orbit represents compositionally and symmetrically equivalent atomic sites sharing the same atom type and Wyckoff position.

We then impose a lexicographical ordering over these orbits, sorting them first by the Pauling electronegativity of their atom type and then by Wyckoff position, as defined in the International Tables for Crystallography (Prince, 2004). Electronegativity provides a chemical signal that correlates with bonding preferences and charge-transfer tendencies, while Wyckoff positions capture crystallographic symmetry with earlier letters indicating higher site symmetry. This ordering injects a soft inductive bias by arranging atoms in a symmetry-aligned and contiguous sequence, enabling the DiT to learn symmetry without explicit conditioning on space group or Wyckoff positions.

**Augmentation via inter- and intra-orbit permutation.**

While the proposed ordering captures compositional and symmetry information, permutation ambiguity remains among tied orbits and atoms within the same orbit. We address this by introducing a hierarchical permutation augmentation scheme that preserves compositional and crystallographic equivalence. For each group of orbits  $\mathcal{W}^i = (O_1^i, \dots, O_m^i)$  sharing the same atom type and Wyckoff position in a primitive unit cell, we apply inter-orbit permutation across orbits followed by intra-orbit permutation within each orbit. This reduces the permutation space from  $N!$  to  $\prod_i |\mathcal{W}^i|! \prod_j |O_j^i|!$ , with a quantitative analysis provided in Appendix D. We additionally apply a global modulo translation to account for translational invariance.

## 4. Experiments

We aim to answer two research questions:

- Can a single MCFlow model achieve competitive performance across crystal structure prediction (CSP), *de novo* generation (DNG), and structure-conditioned atom type generation without task-specific retraining?
- Do the proposed composition- and symmetry-aware atom ordering and symmetry-preserving hierarchical permutation augmentations enable a transformer-based model to capture crystallographic constraints without relying on explicit symmetry templates?

*Table 1. Crystal structure prediction on MP-20 and MPTS-52.* MCFlow shows competitive or superior performance across both benchmarks, with larger gains on MPTS-52 containing larger unit cells. We report match rate (MR) and RMSE for single-sample (1) and multi-sample (20) generation. S/B/L denote small/base/large model sizes. Noisy guidance is applied only for single-sample generation. **Bold** and underline indicate the best overall and best single-sample results, respectively.

Model	MP-20		MPTS-52	
	MR (%) $\uparrow$	RMSE $\downarrow$	MR (%) $\uparrow$	RMSE $\downarrow$
CDVAE (1)	33.90	0.1045	5.34	0.2106
DiffCSP (1)	51.49	0.0631	12.19	0.1786
FlowMM (1)	61.39	0.0566	17.54	0.1726
OMatG (1)	61.88	0.1611	21.70	0.2353
CrystalFlow (1)	62.02	0.0710	22.71	0.1548
DiffCSP (20)	77.93	0.0492	34.02	0.1749
CrystalFlow (20)	<b>78.34</b>	0.0577	40.37	0.1576
MCFlow-S (1)	56.10	0.1269	22.88	0.1845
MCFlow-B (1)	63.14	0.0611	26.46	0.1572
MCFlow-L (1)	<u>64.08</u>	<u>0.0561</u>	<u>27.16</u>	<u>0.1401</u>
MCFlow-S (20)	77.84	0.0939	38.91	0.1717
MCFlow-B (20)	77.12	0.0439	41.40	0.1465
MCFlow-L (20)	76.08	<b>0.0383</b>	<b>41.45</b>	<b>0.1296</b>

To this end, we evaluate MCFlow on all three tasks using the same trained model and conduct ablation studies to assess the contribution of each components. Detailed experimental configurations and metrics are in Appendix F and G.

**Dataset.** Our evaluation uses two inorganic crystal benchmarks: *MP-20* (Xie et al., 2021) and *MPTS-52* (Baird et al., 2024). MP-20 comprises all materials from the Materials Project database (Jain et al., 2013) as of July 2021 that contain no more than 20 atoms per unit cell and reside within 0.08 eV/atom of the convex hull energy. We also test on MPTS-52, a dataset consisting of structures with up to 52 atoms per unit cell. For both datasets, we follow a consistent 60/20/20 ratio for training, validation, and test sets. MPTS-52 dataset is partitioned into time slices based on their initial publication year to reflect a chronological discovery.

**Setup.** MCFlow is based on a Diffusion Transformer (DiT) backbone (Peebles & Xie, 2023) for all-atom crystal modeling. We evaluate three model scales: small (34M parameters, hidden dimension 384, 6 attention heads, 12 layers), base (134M parameters, 768 dimension, 12 heads, 12 layers), and large (464M parameters, 1024 dimension, 16 heads, 24 layers), denoted as MCFlow-S, -B, and -L, respectively. Throughout this paper, MCFlow refers to the base model unless its scale is explicitly stated. Detailed model, training, and inference configurations are provided in Appendix F.

### 4.1. Crystal Structure Prediction

CSP predicts stable crystal structures given a chemical composition: the number of atoms and their types.

**Table 2. De novo generation on the MP-20.** MCFlow achieves competitive performance across most DNG metrics, with strong compositional validity and thermodynamic stability. We report validity, property distribution distances, and stability, uniqueness, and novelty metrics (over valid crystals) for 10,000 generated crystals. Methods evaluated with CHGNet relaxation for stability are denoted by †. MS.U.N. and S.U.N. denote the fraction of valid generated crystals that are unique and novel, and are metastable ( $E_{\text{hull}} < 0.1$  eV/atom) or stable ( $E_{\text{hull}} < 0.0$  eV/atom). NFE denotes the number of function evaluations. **Bold** and underline indicate the best and second-best results. Avg Rank† denotes the average rank across all metrics except NFE, calculated for models evaluated with CHGNet relaxation.

Model	NFE	Validity (%) ↑		Property ↓		Stability, Uniqueness, Novelty (%) ↑				Avg Rank† ↓
		Structural	Compositional	$d_\rho$	$d_{\text{elem}}$	Metastability	MS.U.N.	Stability	S.U.N.	
CDVAE	5000	<b>100.00</b>	86.70	0.688	0.278	-	-	-	-	-
FlowMM	500	96.86	83.24	<b>0.075</b>	0.079	27.3†	22.9†	4.4†	3.3†	3.75
FlowLLM	250	99.81	89.05	0.660	0.090	67.9	21.9	14.2	3.6	-
OMatG	680	99.04	83.40	0.258	<b>0.042</b>	-	-	-	-	-
ADiT	500	99.34	<b>90.76</b>	<u>0.076</u>	0.056	78.9†	14.5†	14.2†	2.7†	3.00
SymmCD	1000	90.34	85.81	0.230	0.400	-	-	-	-	-
DiffCSP++ (+WyFormer)	1000	99.66	80.34	0.670	0.098	-	-	-	3.8	-
SGEquiDiff	1000	99.25	86.16	0.193	0.209	-	<u>25.8</u>	-	-	-
SGFM (+WyFormer)	500	<u>99.87</u>	84.76	0.237	0.233	48.4	22.6	10.6	<u>4.7</u>	-
MCFlow-S	500	99.01	88.23	0.098	0.096	70.3†	<b>41.4†</b>	11.9†	<b>6.1†</b>	3.25
MCFlow-B	500	99.44	89.85	0.136	0.055	87.3†	23.1†	<u>15.1†</u>	3.3†	<b>2.38</b>
MCFlow-L	500	99.61	<u>90.29</u>	0.186	<u>0.046</u>	<b>90.4†</b>	16.8†	<b>16.0†</b>	2.2†	<u>2.50</u>

**Metrics.** Following the metric calculation of Jiao et al. (2023); Miller et al. (2024), we evaluate the accuracy of the generated samples against ground truth structures of test dataset using the StructureMatcher (Ong et al., 2013). We report the Match Rate (MR), defined as the fraction of valid candidates that match their ground truth counterparts. For matched pairs, we also calculate the Root Mean Square Error (RMSE) to assess the precision of the predicted atomic locations within the unit cell.

**Baselines.** We compare MCFlow against baselines: CDVAE (Xie et al., 2021), DiffCSP (Jiao et al., 2023), FlowMM (Miller et al., 2024), CrystalFlow (Luo et al., 2025), and OMatG (Hoellmer et al., 2025). We exclude FlowLLM (Sriram et al., 2024), SymmCD (Levy et al., 2025), and ADiT (Joshi et al., 2025), as they do not support CSP. We also exclude DiffCSP++ (Jiao et al., 2024), SGEquiDiff (Chang et al., 2025), and SGFM (Puny et al., 2025), which rely on structural templates extracted from the target structure or retrieved via CSPML (Kusaba et al., 2022). For a given composition, multiple templates often exist, while one template leads to a nearly unique stable structure (Kazeev et al., 2025), making template-conditioned generation a different problem setting from full CSP. We further compare our method under target-template filtering against these target template-conditioned methods (Appendix H.1).

**Results.** MCFlow achieves competitive performance on MP-20 and shows improved performance on MPTS-52, which contains larger unit cells (Table 1). This improvement reflects the proposed composition- and symmetry-aware ordering and permutation augmentation. MCFlow saturates significantly earlier than FlowMM and DiffCSP in CSP match rate, demonstrating superior sampling efficiency (Figure 3). We also observe consistent scaling behavior across

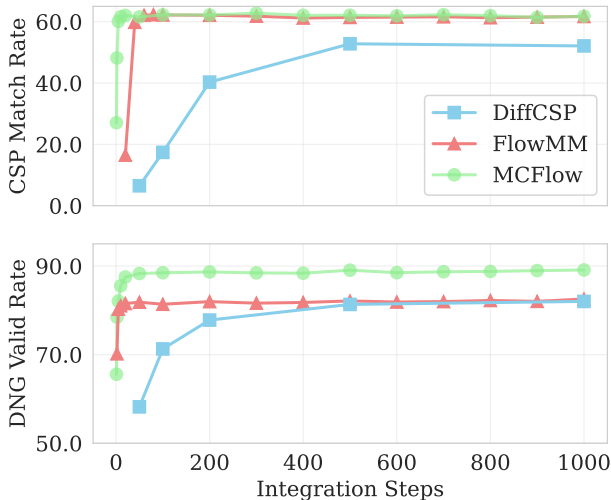


**Figure 3. Effect of the number of integration steps on performance.** Crystal structure prediction (CSP) match rate and *de novo* generation (DNG) validity rate (both structural and compositional) evaluated at different integration steps.

model sizes, as detailed in Appendix H.3. Noisy guidance (NG) further improves single-sample generation accuracy, as demonstrated by the ablation study in Appendix E. Further qualitative samples illustrating diversity given a composition given a composition are provided in Appendix I.

## 4.2. De Novo Generation

In the DNG task, the model generates atom types, lattice parameters, and fractional coordinates at once.

**Metrics.** Structural validity ensures pairwise atomic distances within a crystal are greater than  $0.5\text{\AA}$ , while com-

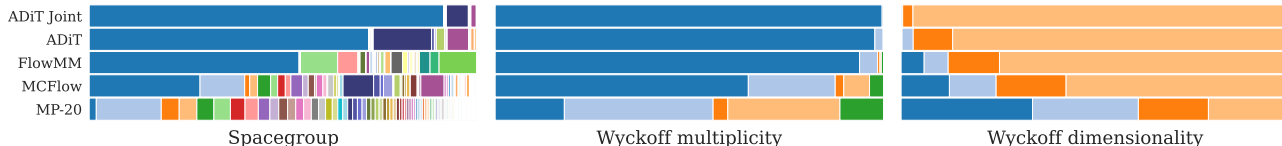


**Figure 4. Distributions of crystallographic symmetry properties.** Distributions of generated structures on MP-20. From left to right, panels show the distributions of space groups (P1, Fm $\bar{3}$ m, C2/m, P6 $\bar{3}$ /mmc, I4/mmm, Pnma, R $\bar{3}$ m, Cmc, Pm $\bar{3}$ m, P4/mmm, P $\bar{1}$ , . . .), Wyckoff multiplicity (1, 2, 3, 4, 6), and Wyckoff dimensionality (0, 1, 2, 3). Space groups and Wyckoff positions are determined using the SpaceGroupAnalyzer module in pymatgen with distance of 0.1 Å.

positional validity is assessed via SMACT (Davies et al., 2019) rules to confirm a neutral charge. We evaluate the statistical fidelity by computing the property metrics  $d_\rho$  and  $d_{\text{elem}}$ , which measure the Wasserstein distance between the generated and test data distributions for density and elemental composition (arity), respectively. We also assess thermodynamic stability by calculating the energy above hull ( $E_{\text{hull}}$ ) with structural relaxation using CHGNet (Deng et al., 2023). We identify a crystal as stable if  $E_{\text{hull}} \leq 0$  eV/atom and as metastable if  $E_{\text{hull}} \leq 0.1$  eV/atom. Finally, we evaluate the quality of generated samples using the stability, uniqueness, and novelty (S.U.N.) and metastability, uniqueness and novelty (MS.U.N.) rates.

**Baselines.** We compare MCFlow against representative crystal generative models, including CDVAE (Xie et al., 2021), FlowMM (Miller et al., 2024), FlowLLM (Sriram et al., 2024), OMatG (Hoellmer et al., 2025), ADiT (Joshi et al., 2025), SymmCD (Levy et al., 2025), DiffCSP++ (Jiao et al., 2024), SGEquiDiff (Chang et al., 2025), and SGFM (Puny et al., 2025). ADiT is trained on MP-20 only. ADiT Joint, which additionally uses QM9 (Wu et al., 2018), is included only in qualitative analysis for reference.

**Results.** MCFlow achieves competitive performance on MP-20 across most metrics, with high accuracy in both compositional validity and thermodynamic stability (Table 2). Notably, MCFlow better captures crystallographic symmetry distributions over space groups and Wyckoff properties, whereas FlowMM and ADiT exhibit mode collapse toward lower-symmetry groups such as P1 (Figure 4). These results indicate that MCFlow internalizes crystallographic symmetry from data without explicit symmetry constraints.

MCFlow also produces geometrically stable samples, with lower structural RMSE and fewer relaxation steps than FlowMM and ADiT, indicating proximity to local energy minima (Figure 5). These structures also exhibit lower  $E_{\text{hull}}$ , reflecting improved thermodynamic stability. MCFlow achieves competitive performance with a relatively small number of integration steps (Figure 3). MCFlow maintains high structural and compositional validity on the larger MPTS-52 dataset (Appendix H.2). While different DNG metrics exhibit varying trends across model sizes, validity shows consistent improvement, as detailed in Appendix H.3.

**Table 3. Atom type generation on MP-20 and MPTS-52.** MCFlow shows higher compositional validity and MR than the baseline when sampling multiple candidates per structure.

Model	MP-20		MPTS-52	
	Comp. (%) $\uparrow$	MR (%) $\uparrow$	Comp. (%) $\uparrow$	MR (%) $\uparrow$
CGCNN	87.06	4.71	82.08	3.50
MCFlow-S (1)	88.97	1.57	83.14	1.01
MCFlow-B (1)	90.17	3.12	83.56	1.20
MCFlow-L (1)	90.07	3.32	83.67	1.24
MCFlow-S (20)	88.71	<b>15.34</b>	83.22	<b>7.22</b>
MCFlow-B (20)	90.22	14.73	84.17	5.72
MCFlow-L (20)	<b>90.23</b>	15.30	<b>84.25</b>	7.20

Additional qualitative samples are provided in Appendix I.

### 4.3. Atom Type Generation

We consider atom type generation task, where we generate atom types conditioned on a crystal structure to demonstrate that the proposed multimodal flow model naturally supports structure-to-composition generation using the same model. This setting reflects a common case in materials datasets, where nearly identical crystal structures can support multiple chemically valid compositions. As a result, it is particularly relevant for exploring atomic substitution patterns within a fixed structure. A deterministic baseline, CGCNN (Xie & Grossman, 2018), is included as a reference point for validity and accuracy.

**Results.** MCFlow generates compositionally valid and diverse atom types when conditioned on a fixed crystal structure. Compared to a deterministic baseline, MCFlow exhibits greater diversity across multiple samples per structure while maintaining high compositional validity, reflecting the probabilistic nature of multimodal flow model (Table 3). Further qualitative samples illustrating compositional diversity in atom type generation are provided in Appendix I. These results illustrate that a single fixed crystal structure can be compatible with multiple valid compositions.

### 4.4. Ablation Studies

We investigate the impact of composition- and symmetry-aware atom ordering and inter- and intra-orbit permutation augmentation to quantify component contributions. We

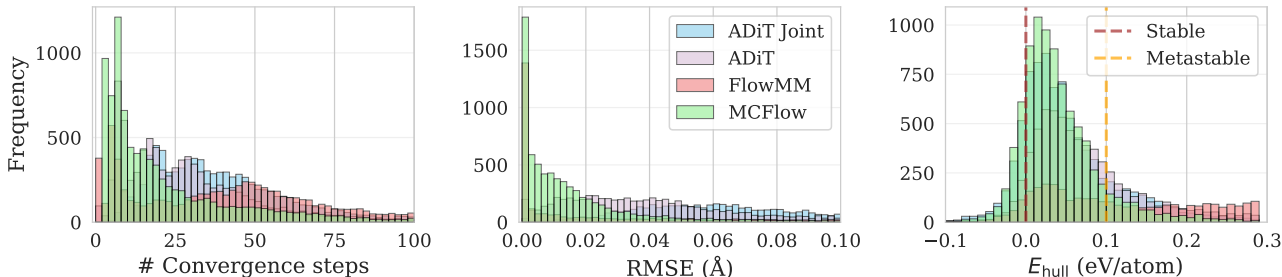


Figure 5. **Distributions of relaxed structures.** Distributions of convergence steps, RMSE between initial and relaxed structures, and  $E_{\text{hull}}$  along CHGNet geometry optimization trajectories, compared to ADiT and FlowMM. The convergence rates are 99.73/60.79/87.65/99.54% for MCFlow/FlowMM/ADiT/ADiT Joint.

Table 4. **Ablation results on MP-20 and MPTS-52.** Rows denote cumulative ablations from the full MCFlow model by removing inter-orbit permutation (– Inter), intra-orbit permutation (– Intra), and positional embedding (– PosEmb). MR and RMSE are reported for CSP, while Struct and Comp denote structural and compositional validity for DNG.

Model	MP-20				MPTS-52			
	MR	RMSE	Struct	Comp	MR	RMSE	Struct	Comp
MCFlow	63.14	0.0611	99.44	89.85	26.46	0.1572	98.34	85.57
– Inter	60.41	0.0772	99.48	89.64	22.80	0.1927	98.12	85.20
– Intra	58.54	0.1023	99.35	89.30	18.80	0.2231	97.70	84.83
– PosEmb	54.83	0.0979	99.48	85.30	16.44	0.2105	98.20	75.20

evaluate these strategies using Match Rate and RMSE for CSP, and structural and compositional validity for DNG.

**Results.** Lexicographical ordering based on electronegativity and Wyckoff position provides compositional and crystallographic priors that are exploited by the DiT model, as shown in Table 4. The PosEmb ablation removes explicit positional information from the sequence representation to assess the contribution of the proposed atom ordering. The resulting performance degradation indicates that the ordering encodes compositional and symmetry information (Table 4). Inter- and intra-orbit permutation augmentation further improves performance by promoting robustness to symmetry-preserving permutations within this ordering.

## 5. Conclusion

We introduced MCFlow, a unified multimodal flow framework that formulates crystal generation tasks as different inference trajectories through a single joint generative model. By decoupling flow time axes for atom types and crystal structures, MCFlow enables flexible conditional generation, allowing crystal structure prediction, *de novo* generation, and atom type generation to be realized within a single model without task-specific architectures or retraining.

To instantiate this unified framework in an all-atom transformer architecture, we proposed a composition- and symmetry-aware atom ordering together with hierarchi-

cal permutation augmentation, providing a soft inductive bias that allows composition and crystallographic symmetry to be learned directly from data without explicit templates. Experiments demonstrate that a single MCFlow model achieves competitive performance across multiple crystal generation tasks, while reducing collapse toward low-symmetry space groups compared to existing baselines.

While MCFlow demonstrates the generality of a unified multimodal flow model, challenges remain in scaling to larger unit cells. Extending the any-to-any formulation to incorporate material property modalities is a natural next step, enabling property-conditioned generation within the same unified multimodal flow framework.

## Impact Statement

MCFlow provides a high-performance computational tool for the discovery of next-generation materials, with potential applications such as solid-state electrolytes for batteries, catalysts for green hydrogen production, and advanced semiconductors. By enabling any-to-any modality generation across atom types and crystal structures within a single model, MCFlow supports a wide range of materials generation tasks without requiring task-specific architectures.

## References

- Baird, S. G., Sayeed, H. M., and Riebesell, J. sparks-baird/matbench-genmetrics. <https://github.com/sparks-baird/matbench-genmetrics>, 2024. [Accessed 03-05-2024].
- Butler, K. T., Davies, D. W., Cartwright, H., Isayev, O., and Walsh, A. Machine learning for molecular and materials science. *Nature*, 559(7715):547–555, 2018.
- Campbell, A., Yim, J., Barzilay, R., Rainforth, T., and Jaakkola, T. Generative flows on discrete state-spaces: Enabling multimodal flows with applications to protein co-design. In *International Conference on Machine Learning*, pp. 5453–5512. PMLR, 2024.
- Cao, Z., Luo, X., Lv, J., and Wang, L. Space group informed transformer for crystalline materials generation, 2024. URL <https://arxiv.org/abs/2403.15734>.
- Cao, Z., Ou, S., and Wang, L. Crystalformer-csp: Thinking fast and slow for crystal structure prediction. *arXiv preprint arXiv:2512.18251*, 2025.
- Chang, R., Pak, A., Guerra, A., Zhan, N., Richardson, N., Ertekin, E., and Adams, R. P. Space group equivariant crystal diffusion. *arXiv preprint arXiv:2505.10994*, 2025.
- Chen, R. T. and Lipman, Y. Riemannian flow matching on general geometries. In *The Twelfth International Conference on Learning Representations*, 2024. URL <https://openreview.net/forum?id=g7ohDl1TITL>.
- Chen, R. T., Rubanova, Y., Bettencourt, J., and Duvenaud, D. K. Neural ordinary differential equations. *Advances in neural information processing systems*, 31, 2018.
- Court, C. J., Yildirim, B., Jain, A., and Cole, J. M. 3-d inorganic crystal structure generation and property prediction via representation learning. *Journal of chemical information and modeling*, 60(10):4518–4535, 2020.
- Dan, Y., Zhao, Y., Li, X., Li, S., Hu, M., and Hu, J. Generative adversarial networks (GAN) based efficient sampling of chemical composition space for inverse design of inorganic materials. *npj Computational Materials*, 6(1):84, 2020.
- Davies, D. W., Butler, K. T., Jackson, A. J., Skelton, J. M., Morita, K., and Walsh, A. SMACT: Semiconducting materials by analogy and chemical theory. *Journal of Open Source Software*, 4(38):1361, 2019.
- Deng, B., Zhong, P., Jun, K., Riebesell, J., Han, K., Bartel, C. J., and Ceder, G. CHGNet as a pretrained universal neural network potential for charge-informed atomistic modelling. *Nature Machine Intelligence*, 5(9):1031–1041, 2023.
- Frank, J. T., Ripken, W., Lied, G., MÄžller, K.-R., Unke, O. T., and Chmiela, S. Sampling 3d molecular conformers with diffusion transformers. *arXiv preprint arXiv:2506.15378*, 2025.
- Glass, C. W., Oganov, A. R., and Hansen, N. Uspeh—evolutionary crystal structure prediction. *Computer physics communications*, 175(11-12):713–720, 2006.
- Grosse-Kunstleve, R. W., Sauter, N. K., and Adams, P. D. Numerically stable algorithms for the computation of reduced unit cells. *Acta Crystallographica Section A: Foundations of Crystallography*, 60(1):1–6, 2004.
- Hiller, H. Crystallography and cohomology of groups. *The American Mathematical Monthly*, 93(10):765–779, 1986.
- Hoellmer, P., Egg, T., Martirosyan, M. M., Fuemmeler, E., Shui, Z., Gupta, A., Prakash, P., Roitberg, A., Liu, M., Karypis, G., Transtrum, M., Hennig, R. G., Tadmor, E. B., and Martiniani, S. Open materials generation with stochastic interpolants, 2025. URL <https://arxiv.org/abs/2502.02582>.
- Hoffmann, J., Maestrati, L., Sawada, Y., Tang, J., Sellier, J. M., and Bengio, Y. Data-driven approach to encoding and decoding 3-d crystal structures. *arXiv preprint arXiv:1909.00949*, 2019.
- Holderrieth, P., Havasi, M., Yim, J., Shaul, N., Gat, I., Jaakkola, T., Karrer, B., Chen, R. T., and Lipman, Y. Generator matching: Generative modeling with arbitrary markov processes. *arXiv preprint arXiv:2410.20587*, 2024.
- Jain, A., Ong, S. P., Hautier, G., Chen, W., Richards, W. D., Dacek, S., Cholia, S., Gunter, D., Skinner, D., Ceder, G., et al. Commentary: The materials project: A materials genome approach to accelerating materials innovation. *APL materials*, 1(1):011002, 2013.
- Jiao, R., Huang, W., Lin, P., Han, J., Chen, P., Lu, Y., and Liu, Y. Crystal structure prediction by joint equivariant diffusion. *arXiv preprint arXiv:2309.04475*, 2023. URL <https://arxiv.org/abs/2309.04475>.
- Jiao, R., Huang, W., Liu, Y., Zhao, D., and Liu, Y. Space group constrained crystal generation, 2024. URL <https://arxiv.org/abs/2402.03992>.
- Joshi, C. K., Fu, X., Liao, Y.-L., Gharakhanyan, V., Miller, B. K., Sriram, A., and Ulissi, Z. W. All-atom diffusion transformers: Unified generative modelling of molecules and materials. In *Forty-second International Conference on Machine Learning*, 2025.
- Kazeev, N., Nong, W., Romanov, I., Zhu, R., Ustyuzhanin, A. E., Yamazaki, S., and Hippalgaonkar, K. Wyckoff

- transformer: Generation of symmetric crystals. In *Forty-second International Conference on Machine Learning*, 2024.
- Kazeev, N., Nong, W., Romanov, I., Zhu, R., Ustyuzhanin, A., Yamazaki, S., and Hippalgaonkar, K. Wyckoff transformer: Generation of symmetric crystals, 2025. URL <https://arxiv.org/abs/2503.02407>.
- Kelvinius, F. E., Andersson, O. B., Parackal, A. S., Qian, D., Armiento, R., and Lindsten, F. Wyckoffdiff—a generative diffusion model for crystal symmetry. In *Forty-second International Conference on Machine Learning*, 2025.
- Kim, S., Noh, J., Gu, G. H., Aspuru-Guzik, A., and Jung, Y. Generative adversarial networks for crystal structure prediction. *ACS central science*, 6(8):1412–1420, 2020.
- Kusaba, M., Liu, C., and Yoshida, R. Crystal structure prediction with machine learning-based element substitution. *Computational Materials Science*, 211:111496, 2022.
- Levy, D., Panigrahi, S. S., Kaba, S.-O., Zhu, Q., Lee, K. L. K., Galkin, M., Miret, S., and Ravanbakhsh, S. Symmcd: Symmetry-preserving crystal generation with diffusion models, 2025. URL <https://arxiv.org/abs/2502.03638>.
- Li, T. and He, K. Back to basics: Let denoising generative models denoise. *arXiv preprint arXiv:2511.13720*, 2025.
- Lipman, Y., Chen, R. T., Ben-Hamu, H., Nickel, M., and Le, M. Flow matching for generative modeling. In *The Eleventh International Conference on Learning Representations*, 2022.
- Lipman, Y., Havasi, M., Holderrieth, P., Shaul, N., Le, M., Karrer, B., Chen, R. T. Q., Lopez-Paz, D., Ben-Hamu, H., and Gat, I. Flow matching guide and code, 2024. URL <https://arxiv.org/abs/2412.06264>.
- Liu, Q. Rectified flow: A marginal preserving approach to optimal transport, 2022. URL <https://arxiv.org/abs/2209.14577>.
- Long, T., Fortunato, N. M., Opahle, I., Zhang, Y., Samathrakris, I., Shen, C., Gutfleisch, O., and Zhang, H. Constrained crystals deep convolutional generative adversarial network for the inverse design of crystal structures. *npj Computational Materials*, 7(1):1–7, 2021.
- Loshchilov, I. and Hutter, F. Decoupled weight decay regularization. *arXiv preprint arXiv:1711.05101*, 2017.
- Luo, X., Wang, Z., Wang, Q., Shao, X., Lv, J., Wang, L., Wang, Y., and Ma, Y. Crystalflow: A flow-based generative model for crystalline materials. *Nature Communications*, 16(1):9267, 2025.
- Miller, B. K., Chen, R. T. Q., Sriram, A., and Wood, B. M. Flowmm: Generating materials with riemannian flow matching, 2024. URL <https://arxiv.org/abs/2406.04713>.
- Nguyen, T. M., Tawfik, S. A., Tran, T., Gupta, S., Rana, S., and Venkatesh, S. Hierarchical gflownet for crystal structure generation. In *AI for Accelerated Materials Design-NeurIPS 2023 Workshop*, 2023.
- Noh, J., Kim, J., Stein, H. S., Sanchez-Lengeling, B., Gregoire, J. M., Aspuru-Guzik, A., and Jung, Y. Inverse design of solid-state materials via a continuous representation. *Matter*, 1(5):1370–1384, 2019.
- Nouira, A., Sokolovska, N., and Crivello, J.-C. Crystalgan: learning to discover crystallographic structures with generative adversarial networks. *arXiv preprint arXiv:1810.11203*, 2018.
- Ong, S. P., Richards, W. D., Jain, A., Hautier, G., Kocher, M., Cholia, S., Gunter, D., Chevrier, V. L., Persson, K. A., and Ceder, G. Python materials genomics (pymatgen): A robust, open-source python library for materials analysis. *Computational Materials Science*, 68:314–319, 2013.
- Peebles, W. and Xie, S. Scalable diffusion models with transformers. In *Proceedings of the IEEE/CVF International Conference on Computer Vision*, pp. 4195–4205, 2023.
- Pickard, C. J. and Needs, R. Ab initio random structure searching. *Journal of Physics: Condensed Matter*, 23(5):053201, 2011.
- Prince, E. *International Tables for Crystallography, Volume C: Mathematical, physical and chemical tables*. Springer Science & Business Media, 2004.
- Puny, O., Lipman, Y., and Miller, B. K. Space group conditional flow matching. *arXiv preprint arXiv:2509.23822*, 2025.
- Ren, Z., Noh, J., Tian, S., Oviedo, F., Xing, G., Liang, Q., Aberle, A., Liu, Y., Li, Q., Jayavelu, S., et al. Inverse design of crystals using generalized invertible crystallographic representation. *arXiv preprint arXiv:2005.07609*, 2020.
- Rojas, K., Zhu, Y., Zhu, S., Ye, F. X., and Tao, M. Diffuse everything: Multimodal diffusion models on arbitrary state spaces. In *Forty-second International Conference on Machine Learning*, 2025.
- Song, Y., Sohl-Dickstein, J., Kingma, D. P., Kumar, A., Ermon, S., and Poole, B. Score-based generative modeling through stochastic differential equations. In *International Conference on Learning Representations*, 2020.

- Sriram, A., Miller, B. K., Chen, R. T., and Wood, B. M. FlowLLM: Flow matching for material generation with large language models as base distributions. In *The Thirty-eighth Annual Conference on Neural Information Processing Systems*, 2024.
- Tangsongcharoen, K., Pakornchote, T., Atthapak, C., Choomphon-anomakhun, N., Ektarawong, A., Alling, B., Sutton, C., Bovornratanaraks, T., and Chotibut, T. Crystalgrw: Generative modeling of crystal structures with targeted properties via geodesic random walks. *arXiv preprint arXiv:2501.08998*, 2025.
- Wang, Y., Lv, J., Zhu, L., and Ma, Y. Crystal structure prediction via particle-swarm optimization. *Physical Review B*, 82(9):094116, 2010.
- Wang, Y., Lv, J., Zhu, L., and Ma, Y. Calypso: A method for crystal structure prediction. *Computer Physics Communications*, 183(10):2063–2070, 2012.
- Wu, Z., Ramsundar, B., Feinberg, E. N., Gomes, J., Geniesse, C., Pappu, A. S., Leswing, K., and Pande, V. Moleculenet: a benchmark for molecular machine learning. *Chemical science*, 9(2):513–530, 2018.
- Wyckoff, R. W. G. *The analytical expression of the results of the theory of space groups*. Number 318. Carnegie institution of Washington, 1930.
- Xie, T. and Grossman, J. C. Crystal graph convolutional neural networks for an accurate and interpretable prediction of material properties. *Physical review letters*, 120(14):145301, 2018.
- Xie, T., Fu, X., Ganea, O.-E., Barzilay, R., and Jaakkola, T. Crystal diffusion variational autoencoder for periodic material generation. *arXiv preprint arXiv:2110.06197*, 2021.
- Yang, M., Cho, K., Merchant, A., Abbeel, P., Schuurmans, D., Mordatch, I., and Cubuk, E. D. Scalable diffusion for materials generation. *arXiv preprint arXiv:2311.09235*, 2023.
- Yi, X., Xu, G., Xiao, X., Zhang, Z., Liu, L., Bian, Y., and Zhao, P. Crystaldit: A diffusion transformer for crystal generation. *arXiv preprint arXiv:2508.16614*, 2025.
- Zeni, C., Pinsler, R., Zügner, D., Fowler, A., Horton, M., Fu, X., Shysheya, S., Crabbé, J., Sun, L., Smith, J., et al. MatterGen: a generative model for inorganic materials design. *arXiv preprint arXiv:2312.03687*, 2023. URL <https://arxiv.org/abs/2312.03687>.
- Zhao, Y., Al-Fahdi, M., Hu, M., Siriwardane, E., Song, Y., Nasiri, A., and Hu, J. High-throughput discovery of novel cubic crystal materials using deep generative neural networks. *arXiv preprint arXiv:2102.01880*, 2021.
- Zhao, Y., Siriwardane, E. M. D., Wu, Z., Fu, N., Al-Fahdi, M., Hu, M., and Hu, J. Physics guided deep learning for generative design of crystal materials with symmetry constraints. *npj Computational Materials*, 9(1):38, 2023. ISSN 2057-3960. doi: 10.1038/s41524-023-00987-9. URL <https://doi.org/10.1038/s41524-023-00987-9>.
- Zhu, R., Nong, W., Yamazaki, S., and Hippalgaonkar, K. Wycryst: Wyckoff inorganic crystal generator framework. *Matter*, 7(10):3469–3488, 2024.

## A. Notations and Backgrounds

Table 5. Summary of Notations

Symbol	Description
$C$	Infinite periodic crystal
$N$	Number of atoms in the primitive unit cell
$A$	Atom types sequence ( $[a_i]_{i=1}^N \in \mathcal{A}^{1 \times N}$ )
$F$	Fractional coordinates ( $[f_i]_{i=1}^N \in [0, 1)^{3 \times N}$ )
$X$	Cartesian coordinates ( $X = LF$ )
$L$	Lattice matrix
$L^l$	Lattice lengths ( $\{a, b, c\} \in \mathbb{R}^{1 \times 3}$ )
$L^a$	Lattice angles ( $\{\alpha, \beta, \gamma\} \in [60^\circ, 120^\circ]^{1 \times 3}$ )
$G$	Space group
$O$	Orbits ( $\{g \cdot f \mid g \in G\}$ )
$G_f$	Site symmetry group ( $\{g \mid g \cdot f = f\}$ )
$\mathcal{W}$	Wyckoff position
$\mathcal{S}$	Discrete state space (e.g., atom type space $\mathcal{A}$ )
$u(x_t, t)$	Velocity field (continuous) or rate vector (discrete)
$p_t$	Probability path at time $t$
$t, s$	Flow time coordinates ( $t$ : atom types, $s$ : structure)
$\pi$	Coupling distribution between $p_0$ and $p_1$
$\delta_{x_t}$	Probability vector with $\delta_{x_t}(x_t) = 1$ on discrete space
$\mathbb{T}^{3 \times N}$	Torus manifold for fractional coordinates ( $\mathbb{R}^{3 \times N} / \mathbb{Z}^{3 \times N}$ )
$\text{proj}(\cdot)$	Projection onto the torus ( $x \pmod{1}$ )

We first formalize periodic crystals and symmetry (space groups, Wyckoff positions), then review flow-based generative models on various state spaces. Table 5 summarizes the key notations used throughout this paper.

### A.1. Crystal Representation

We represent crystals as infinite periodic arrangements of primitive unit cells. The unit cell is represented by atom types  $A = [a_i]_{i=1}^N \in \mathbb{Z}^{1 \times N}$ , fractional coordinates  $F = [f_i]_{i=1}^N \in [0, 1)^{3 \times N}$ , and a lattice matrix  $L = [l_i]_{i=1}^3 \in \mathbb{R}^{3 \times 3}$ . While there are many possible choices of primitive unit cells, we use Niggli reduction (Grosse-Kunstleve et al., 2004) to fix a unique representative. The lattice matrix  $L$  can be also represented as roto-translation invariant lattice parameters: three side lengths  $L^l = \{a, b, c\} \in \mathbb{R}^{1 \times 3}$  and three internal angles  $L^a = \{\alpha, \beta, \gamma\} \in [60^\circ, 120^\circ]^{1 \times 3}$  of the unit cell. Given this lattice representation  $L$ , the 3D Cartesian coordinates  $X = [x_i]_{i=1}^N \in \mathbb{R}^{3 \times N}$  are obtained by the linear combination of lattice vectors with fractional coefficients:  $X = LF$ . The infinite periodic crystal  $C$  is then defined as:

$$C = \{(a_i, x_i + Lk) \mid i \in \{1, \dots, N\}, k \in \mathbb{Z}^3\} \quad (12)$$

where  $k_j$  denotes the integral translation along the  $j$ -th lattice vector  $l_j$ .

### A.2. Crystal Symmetry

Space groups (Hiller, 1986) characterize the invariances of infinite periodic structures.

**Space groups.** A space group  $G$  is a group of isometries that tile  $\mathbb{R}^3$  with repeating unit cells, i.e., a set of operation  $g$  under which the transformed crystal  $C$  is identical to the original crystal where operation  $g = (R, t) \in G$  consists of an orthogonal matrix  $R \in O(3)$  and a translation  $t \in \mathbb{R}^3$ . Its action on a Cartesian coordinate  $x \in \mathbb{R}^3$  denotes  $g \cdot x := Rx + t$ . When expressed in fractional coordinates  $f$  with  $x = Lf$ , we use the corresponding induced action

$$g \cdot f := L^{-1}(R(Lf) + t) \pmod{1}, \quad (13)$$

where  $\pmod{1}$  is applied component-wise, identifying fractional coordinates that differ by lattice translations. A space group operation first acts on atomic positions in Cartesian space and then maps the result back into the unit cell via fractional coordinates modulo lattice translations.

A crystal  $C$  is said to be invariant under space group  $G$  if for every  $g \in G$ , there exists a permutation  $\sigma_g \in S_N$  of the atom indices such that the transformed atomic positions coincide with the original ones up to lattice translations and a permutation of atom indices preserving atom types. This permutation  $\sigma_g$  rearranges indices changed by the symmetry operation  $g$  while preserving their atom types. Every crystal has space group symmetry which is one of the 230 distinct space groups, a unique way a crystal’s atoms can be arranged periodically.

**Wyckoff positions.** Given a space group  $G$ , Wyckoff positions (Wyckoff, 1930) describe crystal symmetry at the level of atomic sites. For a fractional coordinate  $f$ , a set of equivalent atoms generated by group  $G$ , called *orbit*, is

$$G \cdot f := \{g \cdot f \mid g \in G\},$$

*Site symmetry group* of  $f$  is a subgroup of the space group consisting of operations that leave the site invariant (up to lattice translations):

$$G_f := \{g \in G \mid g \cdot f = f\}.$$

We can classify site symmetry groups based on conjugate relation, which is equivalent relation, up to basis change by space group, between  $G_f$  and  $G_{f'}$  defined by  $G_{f'} = gG_f g^{-1}$  for some  $g \in G$ . The conjugate relation induces an equivalence class  $[G_f]$  of site symmetry groups

$$[G_f] := \{gG_f g^{-1} \mid g \in G\}.$$

*Wyckoff position* is a set of orbits whose site symmetry groups have conjugate relation:

$$\mathcal{W}_{[G_f]} := \{G \cdot f' \mid G_{f'} \in [G_f]\}.$$

The size of its orbit  $|G \cdot f|$  is called the *Wyckoff multiplicity*. Wyckoff positions are conventionally labeled by letters  $a, b, c, \dots$ , called the *Wyckoff letter*. The letter is assigned according to the site symmetry following the IUCr convention (Prince, 2004). Ordering atoms by Wyckoff position encodes crystallographic symmetry information that is useful for transformer models.

### A.3. Flow Generative Model

We provide a self-contained background on flow-based models and flow matching in various state spaces. For a more comprehensive guide and practical implementation details of flow matching, we refer the reader to Lipman et al. (2024). Flow models naturally extend to multimodal settings by combining continuous and discrete state spaces under a unified generator matching framework (Holderrith et al., 2024).

**Flow-based generative model.** Flow-based generative model (Chen et al., 2018), or simply flow model, transports a base distribution  $p_0(x_0) = p_{\text{base}}$  to data distribution  $p_1(x_1) = p_{\text{data}}$  by solving an ordinary differential equation (ODE) characterized by a time-dependent velocity field  $u(x_t, t)$  for  $t \in [0, 1]$ :

$$\frac{dx_t}{dt} = u(x_t, t), \quad x_0 \sim p_0. \quad (14)$$

Flow models construct and learn  $u(x_t, t)$  which corresponds to probability path  $\{p_t\}_{t \in [0,1]}$  evolving from  $p_0 = p_{\text{base}}$  to  $p_1 = p_{\text{data}}$ .

**Flow matching.** Flow matching (FM) is a simulation-free training method to learn the constructed velocity field  $u(x_t, t)$  (Lipman et al., 2022; Liu, 2022). Given a neural network  $u_\theta(x_t, t)$ , the objective is to minimize the squared distance

$$\mathcal{L}_{\text{FM}}(\theta) = \mathbb{E}_{t, x_t} [\|u_\theta(x_t, t) - u(x_t, t)\|^2], \quad (15)$$

where  $t \sim \mathcal{U}[0, 1]$  and  $x_t \sim p_t$ . Lipman et al. (2022) defines the probability path as a mixture of tractable conditional probability paths  $p_t(\cdot | x_0, x_1)$ :

$$p_t(x) = \int p_t(x | x_0, x_1) d\pi(x_0, x_1), \quad (16)$$

where  $\pi(x_0, x_1)$  is a independent coupling distribution over the base and data distributions, i.e.,  $\pi(x_0, x_1) = p_0(x_0)p_1(x_1)$ . Lipman et al. (2022) introduces conditional flow matching (CFM) which minimizes the distance between  $u_\theta(x_t, t)$  with tractable conditional velocity field  $u(x_t, t | x_0, x_1)$ :

$$\mathcal{L}_{\text{CFM}}(\theta) = \mathbb{E}_{t, x_0, x_1, x_t} [\|u_\theta(x_t, t) - u(x_t, t | x_0, x_1)\|^2], \quad (17)$$

where pairs  $(x_0, x_1)$  are sampled from the coupling distribution  $\pi(x_0, x_1)$ , and conditional flow  $x_t$  is sampled from conditional probability path  $p_t(\cdot|x_0, x_1)$ . The conditional flow matching objective induces the same gradient with respect to  $\theta$  as the marginal flow matching objective, i.e.,  $\nabla_{\theta} \mathcal{L}_{\text{FM}}(\theta) = \nabla_{\theta} \mathcal{L}_{\text{CFM}}(\theta)$

A simple and commonly used conditional flow is linear interpolation  $x_t = (1-t)x_0 + tx_1$  between two endpoints  $x_0$  and  $x_1$ , corresponding to the conditional velocity field:

$$u(x_t, t | x_0, x_1) = \frac{x_1 - x_0}{1-t}. \quad (18)$$

We can construct the marginal velocity field  $u(x_t, t)$ , constructed via posterior expectation over  $\pi$ :

$$u(x_t, t) = \mathbb{E}_{x_0, x_1} [u(x_t, t | x_0, x_1) | x_t], \quad (19)$$

ensuring transports from  $p_0$  to  $p_1$ . The CFM objective extends the squared distance loss to a Bregman divergence  $D_{\Phi}(u, v) = \Phi(u) - \Phi(v) - \langle \nabla \Phi(v), u - v \rangle$ :

$$\mathbb{E}_{t, x_0, x_1, x_t} [D(u_{\theta}(x_t, t), u(x_t, t | x_0, x_1))], \quad (20)$$

where  $\Phi$  is a convex function. Bregman divergences are used since they preserve the gradient equivalence between conditional and marginal flow matching objectives. This formulation allows different choices of  $\Phi$  and recovers the squared distance loss  $D(u, v) = \|u - v\|^2$  when  $\Phi(u) = \|u\|^2$ .

**Riemannian flow model.** The above flow model assumes that data lie in Euclidean space. When data distribution is on Riemannian manifold  $\mathcal{M}$ , Riemannian flow model (Chen & Lipman, 2024) transports base distribution on the manifold to the data distribution with velocity field  $u(x_t, t)$  in tangent space  $T_{x_t}\mathcal{M}$ . The construction  $u(x_t, t)$  from the conditional velocity field  $u(x_t, t | x_0, x_1)$  is obtained by replacing straight-line paths with geodesics:  $x_t = \exp_{x_0}(t \log_{x_0}(x_1))$  where  $\exp_x$  and  $\log_x$  denote the Riemannian exponential and logarithmic maps. The corresponding conditional velocity field is

$$u(x_t, t | x_0, x_1) = \frac{\log_{x_t}(x_1)}{1-t} \in T_{x_t}\mathcal{M}. \quad (21)$$

Flow matching regresses  $u_{\theta}(x_t, t)$  onto the target  $u(x_t, t | x_0, x_1)$  in the tangent space. A commonly used Bregman divergence is  $D(u, v) = \|u - v\|_g^2$  for a Riemannian metric  $g$  on the manifold  $\mathcal{M}$ .

**Discrete flow model.** To extend flow models on continuous space to flow model on discrete state space  $\mathcal{S}$ , we convert solving ODE with the velocity field  $u(x_t, t)$  into transition probability vector  $p_{t+h|t}(\cdot | x_t)$  from current state  $x_t$  for small increment  $h > 0$ , called continuous-time Markov chain (CTMC):

$$p_{t+h|t}(\cdot | x_t) = \delta_{x_t} + h u(x_t, t) + o(h), \quad (22)$$

where rate vector  $u(x_t, t)$  governs CTMC and  $\delta_{x_t}$  is the probability vector for current state  $x_t$  which satisfies  $\delta_{x_t}(x_t) = 1$  and  $\delta_{x_t}(x) = 0$  if  $x \neq x_t$ . Discrete flow model aims to learn the rate vector  $u(x_t, t)$  which transports the base probability vector  $p_0$  to the data probability vector  $p_1$  through probability vector path  $\{p_t\}_{t \in [0,1]}$ . We use masked flow model where the base probability vector  $p_0 = \delta_M$  for the masked state  $M$ .

**Discrete flow matching.** Analogous to the continuous case, we match the parameterized and target rate vectors,  $u_{\theta}(x_t, t)$  and  $u(x_t, t)$ , respectively, given the current state  $x_t$ . A commonly used Bregman divergence is the generalized KL divergence  $D(u, v) = \sum_j u_j \log(u_j/v_j) - \sum_j u_j + \sum_j v_j$  and the FM objective has the same form with Equation (20) where marginal rate vector are constructed by conditional rate vector as in Equation (19). Discrete flow model also extends to CFM objective for tractability. A commonly used conditional probability vector path is the independent mixture path between the base state  $x_0 = M$  and the target state  $x_1$  sampled from  $p_1$ :

$$p_t(\cdot | x_0, x_1) = (1-t)\delta_{x_0} + t\delta_{x_1}, \quad (23)$$

which is the discrete analog of linear interpolation. The corresponding conditional rate vector is given by:

$$u(x_t, t | x_0, x_1) = \frac{\delta_{x_0}(x_t)\delta_{x_1}}{1-t}. \quad (24)$$

where  $x_0 = M$ . While continuous and discrete flow matching are defined on different frameworks, ODE and CTMC, they can be unified into generator matching on continuous-time Markov process (Holderrieth et al., 2024). This unifying perspective enables joint generative processes in which continuous and discrete dynamics evolve simultaneously over different components of the state space.

**Table 6. Configurations for Multimodal Flow Matching.** We leverage the flexibility of the flow matching framework to design components for each modality. The Base dist. column specifies the prior distribution  $p_0$ , selected to match the support of each modality. The Cond. target column defines the conditional target vector fields or rate vectors derived from data pairs, utilizing linear interpolation for Euclidean space, geodesic paths for the torus, and independent mixture paths for discrete atom types. The Parameterization column describes how to approximate the target velocity field from the clean data prediction ( $F_\theta, L_\theta^l, L_\theta^a$ ) or the target categorical posterior distribution via atom type logit prediction  $A_\theta$ . Finally, the Bregman div. column lists the specific divergence metric minimized during training to match the parameterized and target velocity field or rate vector. Since the torus is flat and locally Euclidean, the Bregman divergence on fractional coordinates is the squared Euclidean distance in the tangent space.

Modality ( $m$ )	Base dist. $p_0$	Cond. target	Parameterization $u_\theta^m$	Bregman div. $D_m(u, v)$
Atom type ( $A$ )	$\delta_M$	$\frac{\delta_{A_0}(A_t)\delta_{A_1}}{1-t}$	$\frac{\delta_{A_0}(A_t)\text{Cat}(\text{softmax}(A_\theta))}{1-t}$	$\sum_j u_j \log\left(\frac{u_j}{v_j}\right) - \sum_j u_j + \sum_j v_j$
Frac. coord. ( $F$ )	$\mathcal{U}[0, 1]^{3 \times N}$	$\frac{\log_{F_s}(F_1)}{1-s}$	$\frac{\log_{F_s}(\text{proj}(F_\theta))}{1-s}$	$\ u - v\ ^2$
Length ( $L^l$ )	$\text{LogNorm}(\mu, \sigma)$	$\frac{L_1^l - L_s^l}{1-s}$	$\frac{L_\theta^l - L_s^l}{1-s}$	$\ u - v\ ^2$
Angle ( $L^a$ )	$\mathcal{U}[60^\circ, 120^\circ]^{1 \times 3}$	$\frac{L_1^a - L_s^a}{1-s}$	$\frac{L_\theta^a - L_s^a}{1-s}$	$\ u - v\ ^2$

## B. Multimodal Flow Details

We provide detailed configurations for each modality in Table 6.

**Riemannian flow on the torus for fractional coordinates.** We model fractional coordinates  $F$  on the torus manifold  $\mathbb{T}^{3 \times N}$  to enforce the periodicity of crystal structures. The corresponding Riemannian exponential and logarithmic maps are given by

$$\exp_f(v) = (f + v) \pmod{1}, \quad \log_f(f') = \frac{1}{2\pi} \text{atan2}(\sin(2\pi(f' - f)), \cos(2\pi(f' - f))). \quad (25)$$

This Riemannian formulation ensures that generated fractional coordinates remain within the fundamental domain  $[0, 1)$  by construction.

**Parameterization details.** We use  $x_1$ -prediction across all modalities and convert the predicted clean data into velocity fields or rate vectors according to the underlying state space of each modality. For lattice lengths and angles in Euclidean space, the network outputs  $L_\theta^l$  and  $L_\theta^a$ , which are converted to conditional velocity targets via  $(L_\theta^l - L_s^l)/(1-s)$  and  $(L_\theta^a - L_s^a)/(1-s)$ , respectively. For fractional coordinates on the torus  $\mathbb{T}^{3 \times N}$ , the network predicts  $F_\theta$ , which is first projected component-wise onto the torus via  $\text{proj}(F) = F \pmod{1}$ . The velocity field is then obtained by applying the logarithmic map on the torus,  $\log_{F_s}(\text{proj}(F_\theta))/(1-s)$ , ensuring that the resulting flow respects the periodic topology of fractional coordinates. For discrete atom types, the network predicts logits  $A_\theta$  corresponding to the target atom types  $A_1$ . These logits define a posterior categorical distribution  $p_\theta = \text{Cat}(\text{softmax}(A_\theta))$ , which induces the rate vector of the CTMC as  $\delta_{A_0}(A_t)p_\theta/(1-t)$ . To mitigate numerical instability near the terminal times, we clip the flow times  $t$  and  $s$  to 0.9 during training, following [Campbell et al. \(2024\)](#).

**Base distribution details.** For lattice lengths, the parameters of the LogNormal prior are fitted to training data statistics via maximum likelihood. During inference, the number of atoms  $N$  is sampled from the empirical distribution of the training dataset, which determines the dimensionality of the base distribution.

## C. Algorithm

---

**Algorithm 1** MCFlow preprocessing and training
 

---

- 1: **Input:** dataset  $\mathcal{D}$ , clean data (and logit) prediction network  $f_\theta$ , joint base dist.  $p_0$ , weights  $\{w_m\}_{m \in \{A, F, L^a, L^l\}}$ .
- 2: **Preprocessing:**
- 3: Group atoms into orbits for each crystal in  $\mathcal{D}$ .
- 4: Sort orbits lexicographically by electronegativity and Wyckoff position for each crystal.
- Training:**
- 5: Sample  $(A_1, X_1) \sim \mathcal{D}$  where  $X_1 = (F_1, L_1^l, L_1^a)$ .
- 6: Apply inter- and intra-orbit permutations.
- 7: Apply global modulo translation.
- 8: Sample  $t, s \sim \mathcal{U}[0, 1]$  and  $(A_0, F_0, L_0^l, L_0^a) \sim p_0(A_0, X_0)$ .
- 9: Sample (or evaluate) intermediates from endpoint-conditioned paths:

$$A_t \sim \text{Cat}((1-t)\delta_{A_0} + t\delta_{A_1}), \quad F_s \leftarrow \exp_{F_0}(s \log_{F_0}(F_1)), \quad L_s^l \leftarrow (1-s)L_0^l + sL_1^l, \quad L_s^a \leftarrow (1-s)L_0^a + sL_1^a.$$

- 10: Construct modality-wise conditional target velocity field or rate vector:

$$u^A = \frac{\delta_{A_0}(A_t)\delta_{A_1}}{1-t}, \quad u^F \leftarrow \frac{\log_{F_s}(F_1)}{1-s}, \quad u^{L^l} \leftarrow \frac{L_1^l - L_s^l}{1-s}, \quad u^{L^a} \leftarrow \frac{L_1^a - L_s^a}{1-s}.$$

- 11: Predict  $(A_\theta, F_\theta, L_\theta^l, L_\theta^a) \leftarrow f_\theta(A_t, X_s, t, s)$ .
- 12: Compute rate vector for atom types and velocity fields for crystal structure:

$$u_\theta^A \leftarrow \frac{\delta_{A_0}(A_t)\text{Cat}(\text{softmax}(A_\theta))}{1-t}, \quad u_\theta^F \leftarrow \frac{\log_{F_s}(\text{proj}(F_\theta))}{1-s}, \quad u_\theta^{L^l} \leftarrow \frac{L_\theta^l - L_s^l}{1-s}, \quad u_\theta^{L^a} \leftarrow \frac{L_\theta^a - L_s^a}{1-s}$$

- 13: Compute the multimodal flow matching objective:

$$\widehat{\mathcal{L}}(\theta) = \sum_{m \in \{A, F, L^a, L^l\}} w_m D_m(u_\theta^m, u^m),$$

- 14: Update parameters  $\theta$  using AdamW with learning rate  $\eta$ .
-

---

**Algorithm 2** MCFlow any-to-any modality generation (DNG/CSP/ATG) during inference

---

- 1: **Input:** trained model  $\text{MCFlow}_\theta$ , timesteps  $K$ , empirical atom-count distribution  $p_{\text{emp}}(N)$ .
  - 2: **Input:** task  $\tau \in \{\text{DNG}, \text{CSP}, \text{ATG}\}$  with atom types  $A_1$  (CSP); structure  $X_1$  (ATG).
  - 3: **Output:** a sample  $(A, X)$ .
  - 4: Set task-specific trajectory  $\gamma$  and conditioning set  $\mathcal{C}$ .
  - 5: **if**  $\tau = \text{DNG}$ :  $\gamma(\lambda) = (\lambda, \lambda)$ ,  $\mathcal{C} \leftarrow \emptyset$ .
  - 6: **if**  $\tau = \text{CSP}$ :  $\gamma(\lambda) = (1, \lambda)$ ,  $\mathcal{C} \leftarrow \{A\}$ .
  - 7: **if**  $\tau = \text{ATG}$ :  $\gamma(\lambda) = (\lambda, 1)$ ,  $\mathcal{C} \leftarrow \{X\}$ .
  - 8: Fix observed modality:  $A \leftarrow A_1$  if  $\tau = \text{CSP}$ ;  $X \leftarrow X_1$  if  $\tau = \text{ATG}$ .
  - 9: Set  $N \leftarrow \text{sample } p_{\text{emp}}(N)$  if  $\tau = \text{DNG}$ ; otherwise  $N = |A_1|$  (CSP) or  $N = |X_1|$  (ATG).
  - 10: **If**  $A \notin \mathcal{C}$ , sample  $A \sim p_0(A)$ .
  - 11: **If**  $X \notin \mathcal{C}$ , sample  $X \sim p_0(X)$ .
  - 12: **for**  $k = 0$  **to**  $K - 1$  **do**
  - 13:    $(t_k, s_k) \leftarrow \gamma(k/K)$ ;    $(t_{k+1}, s_{k+1}) \leftarrow \gamma((k+1)/K)$
  - 14:    $\Delta t \leftarrow t_{k+1} - t_k$ ;    $\Delta s \leftarrow s_{k+1} - s_k$
  - 15:    $(u_\theta^A, u_\theta^X) \leftarrow \text{MCFlow}_\theta(A, X, t_k, s_k)$
  - 16:   **If**  $A \notin \mathcal{C}$ ,  $A \leftarrow \text{CTMCStep}(A, u_\theta^A, \Delta t)$ .
  - 17:   **If**  $X \notin \mathcal{C}$ ,  $X \leftarrow \text{ODEStep}(X, u_\theta^X, \Delta s)$ .
  - 18: **end for**
  - 19: **return**  $(A, X)$ .
-

---

**Algorithm 3** MCFlow inference with noisy guidance (CSP/ATG)

---

- 1: **Input:** timesteps  $K$ , guidance scale  $\omega$ , noise level  $\sigma$ .
  - 2: **Input:** task  $\tau \in \{\text{CSP}, \text{ATG}\}$  with atom types  $A_1$  (CSP); structure  $X_1$  (ATG).
  - 3: **Output:** a guided sample  $(A, X)$ .
  - 4: Set task-specific trajectory  $\gamma$  and conditioning set  $\mathcal{C}$ .
  - 5: **if**  $\tau = \text{CSP}$ :  $\gamma(\lambda) = (1, \lambda)$ ,  $\mathcal{C} \leftarrow \{A\}$ .
  - 6: **if**  $\tau = \text{ATG}$ :  $\gamma(\lambda) = (\lambda, 1)$ ,  $\mathcal{C} \leftarrow \{X\}$ .
  - 7: Fix observed modality:  $A \leftarrow A_1$  if  $\tau = \text{CSP}$ ;  $X \leftarrow X_1$  if  $\tau = \text{ATG}$ .
  - 8: Set  $N \leftarrow |A_1|$  (CSP) or  $N \leftarrow |X_1|$  (ATG).
  - 9: **if**  $\tau = \text{CSP}$ : sample  $X \sim p_0(X)$ .
  - 10: **if**  $\tau = \text{ATG}$ : sample  $A \sim p_0(A)$ .
  - 11: **for**  $k = 0$  **to**  $K - 1$  **do**
  - 12:    $(t_k, s_k) \leftarrow \gamma(k/K)$ ;    $(t_{k+1}, s_{k+1}) \leftarrow \gamma((k+1)/K)$
  - 13:    $\Delta t \leftarrow t_{k+1} - t_k$ ;    $\Delta s \leftarrow s_{k+1} - s_k$
  - 14:   **if**  $\tau = \text{CSP}$ :
  - 15:     Sample  $A_0 \sim p_0(A)$  and  $A_\sigma \sim \text{Cat}((1 - \sigma)\delta_{A_0} + \sigma\delta_{A_1})$
  - 16:      $u_{\text{cond}}^X \leftarrow u_\theta^X(A_1, X, 1, s_k)$ ;    $u_{\text{corr}}^X \leftarrow u_\theta^X(A_\sigma, X, \sigma, s_k)$
  - 17:      $u_{\text{ng}}^X \leftarrow (1 - \omega) u_{\text{corr}}^X + \omega u_{\text{cond}}^X$
  - 18:      $X \leftarrow \text{ODEStep}(X, u_{\text{ng}}^X, \Delta s)$
  - 19:   **if**  $\tau = \text{ATG}$ :
  - 20:     Sample  $X_0 \sim p_0(X)$  and  $X_\sigma \sim p_\sigma(X_\sigma | X_0, X_1)$
  - 21:      $u_{\text{cond}}^A \leftarrow u_\theta^A(A, X_1, t_k, 1)$ ;    $u_{\text{corr}}^A \leftarrow u_\theta^A(A, X_\sigma, t_k, \sigma)$
  - 22:      $u_{\text{ng}}^A \leftarrow (1 - \omega) u_{\text{corr}}^A + \omega u_{\text{cond}}^A$
  - 23:      $A \leftarrow \text{CTMCStep}(A, u_{\text{ng}}^A, \Delta t)$
  - 24: **end for**
  - 25: **return**  $(A, X)$ .
-

## D. Ordering and Augmentation Analysis

**Permutation space reduction analysis.** To quantify the impact of our hierarchical permutation augmentation, we evaluate search space complexity in the MP-20 training dataset. For each crystal structure, we calculate the size of the reduced permutation space using the formula  $\prod_i |\mathcal{W}^i|! \prod_j |O_j^i|!$ , where  $i$  denotes groups sharing the same element and Wyckoff position, and  $j$  denotes individual orbits within those groups. We then group these values by the number of atoms in the unit cell ( $N$ ) and calculate the minimum, median, and maximum values for each group to capture the distribution across different symmetry.

Figure 6 illustrates the size of the permutation space as a function of  $N$ . While the naive permutation space grows factorially as  $N!$ , our proposed ordering combined with the hierarchical augmentation constraints drastically restricts the residual freedom. As shown in the figure, for a unit cell with  $N = 20$  atoms, the median reduced space size is approximately  $10^{7.2}$ , whereas the full permutation space is  $20! \approx 10^{18.4}$ . This reduction of over 11 orders of magnitude provides a strong inductive bias, enabling the Diffusion Transformer to effectively learn crystallographic symmetry and compositional priors directly from data without explicit structural templates.

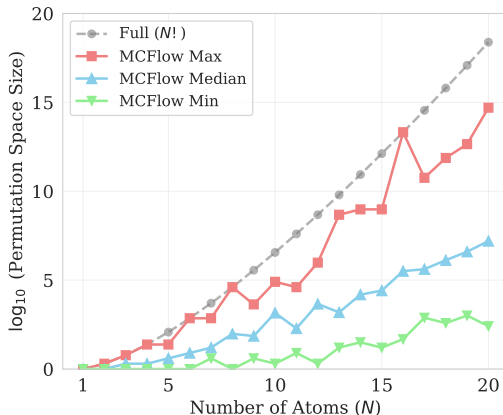


Figure 6. **Permutation space reduction.** Logarithmic scale comparison of full permutation space  $N!$  and reduced space  $\prod_i |\mathcal{W}^i|! \prod_j |O_j^i|!$  across unit cell sizes  $N = 1$  to 20.

Table 7. Ablation study of noisy guidance on CSP and atom type generation (ATG). Single-sample generation per composition or structure. **Bold** indicate the best performance within each model size group. Noisy guidance improves structural fidelity in CSP and yields competitive performance in ATG across datasets.

Model	NG	CSP				ATG			
		MP-20		MPTS-52		MP-20		MPTS-52	
		MR (%) $\uparrow$	RMSE $\downarrow$	MR (%) $\uparrow$	RMSE $\downarrow$	Comp. (%) $\uparrow$	MR (%) $\uparrow$	Comp. (%) $\uparrow$	MR (%) $\uparrow$
MCFlow-S	$\times$	54.40	0.1339	22.58	0.1880	88.89	1.53	<b>83.19</b>	0.98
MCFlow-S	$\checkmark$	<b>56.10</b>	<b>0.1269</b>	<b>22.88</b>	<b>0.1845</b>	<b>88.97</b>	<b>1.57</b>	83.14	<b>1.01</b>
MCFlow-B	$\times$	62.11	0.0624	25.32	0.1640	90.05	2.69	<b>84.29</b>	1.09
MCFlow-B	$\checkmark$	<b>63.14</b>	<b>0.0611</b>	<b>26.46</b>	<b>0.1572</b>	<b>90.17</b>	<b>3.12</b>	83.56	<b>1.20</b>
MCFlow-L	$\times$	63.86	<b>0.0546</b>	26.63	0.1499	<b>90.17</b>	3.21	<b>84.67</b>	<b>1.33</b>
MCFlow-L	$\checkmark$	<b>64.08</b>	0.0561	<b>27.16</b>	<b>0.1401</b>	90.07	<b>3.32</b>	83.67	1.24

### E. Noisy Guidance

**Noisy guidance for atom type generation.** For atom type generation, we apply noisy guidance at the logit level of the categorical distribution, which induces guided rate vector for the corresponding CTMC.

**Ablation study.** We perform an ablation study on single-sample CSP to evaluate the effect of noisy guidance. Table 7 shows that applying noisy guidance generally improves the match rate and RMSE on CSP across MP-20 and MPTS-52, indicating enhanced structural fidelity.

**Sensitivity to noise level and guidance scale.** Figure 7 analyzes the sensitivity of noisy guidance to the atom-type noise level  $\sigma$  and guidance scale  $\omega$  on single-sample CSP. We observe that introducing a small amount of noise ( $\sigma > 0$ ) consistently improves both match rate and RMSE compared to the noiseless setting. Performance peaks at low noise levels  $\sigma = 0.1$ , while larger noise gradually degrades structural accuracy. While the method remains robust across a range of guidance scales, we observe that  $\omega = 2.0$  consistently yields strong performance.

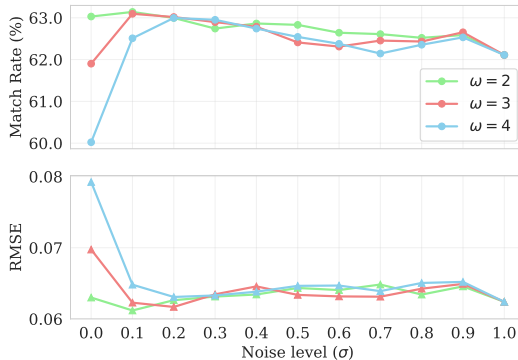


Figure 7. Sensitivity analysis of noisy guidance. Single-sample CSP performance on MP-20 depending on the atom type noise level  $\sigma$  and guidance scale  $\omega$ .

## F. Model and Training Configurations

We provide detailed settings of model architectures (Table 8), training (Table 9), and inference (Table 10) used in our experiments to ensure reproducibility.

Table 8. MCFlow model configurations.

Model scale	Small (S)	Base (B)	Large (L)
# Parameters	34M	134M	464M
Hidden dimension	384	768	1024
Transformer layers	12	12	24
Attention heads	6	12	16

**Training settings.** We train all models for a maximum of 10,000 epochs using the AdamW optimizer (Loshchilov & Hutter, 2017) with a constant learning rate of  $1 \times 10^{-4}$  and no weight decay. To balance learning dynamics across different modalities, we set the loss weights to 0.5 for atom types, 2.0 for fractional coordinates, and 1.0 for lattice parameters. The batch size is set to 256. For computational efficiency, all models are trained using Bfloat16 (BF16) mixed precision. To ensure training stability, we apply gradient clipping with a maximum norm of 10.0 and clip flow times  $t, s$  to 0.9 to mitigate numerical instability near the boundaries (Campbell et al., 2024). Additionally, we maintain an exponential moving average (EMA) of the model weights with a decay rate of 0.9999. The final model is selected by taking the latest epoch among the top three checkpoints ranked by total validity (structural and compositional) on the validation set.

Table 9. MCFlow training configurations.

Hyperparameter	Value
Optimizer	AdamW
Learning rate	$1 \times 10^{-4}$
Weight decay	0.0
Batch size	256
Max epochs	10,000
Precision	BF16 mixed precision
Gradient clipping	max norm 10.0
EMA decay	0.9999
Flow time clipping	$t, s \leq 0.9$
Loss weights ( $A/F/L^l/L^a$ )	0.5 / 2.0 / 1.0 / 1.0

**Inference settings.** During sampling, we solve the probability flow ODE for continuous variables and simulate the CTMC for discrete variables using 500 integration steps to generate crystals. To improve sample fidelity in single-sample CSP and structure-conditioned atom type generation, we apply noisy guidance with a guidance scale  $\omega = 2.0$  and a noise level  $\sigma = 0.1$ . In contrast, for 20-sample generation, we disable noisy guidance to better capture the multimodal nature of the distribution. The number of atoms is sampled from the empirical distribution of atom counts in the training set.

Table 10. MCFlow inference configurations.

Hyperparameter	Value
Integration steps	500
Guidance scale $\omega$	2.0 (single-sample)
Noise level $\sigma$	0.1 (single-sample)

**Computational resources.** All experiments for the Small and Base models were conducted on a single NVIDIA GeForce RTX 3090 GPU, while experiments for the Large model were conducted on a single NVIDIA A40 GPU. Training the Base model takes approximately 2 days on MP-20 and 4 days on MPTS-52.

## G. Evaluation Metrics

We summarize the evaluation metrics used in MCFlow, following prior work on crystal generation (Xie et al., 2021; Miller et al., 2024).

**Crystal Structure Prediction.** We compare generated structures against ground-truth test structures using `StructureMatcher` from `pymatgen` (Ong et al., 2013). The Match Rate (MR) is the fraction of generated candidates that match their corresponding ground-truth structures under symmetry-aware matching with tolerances `stol=0.5`, `ltol=0.3`, and `angle_tol=10°`. For matched pairs only, we compute the Root Mean Square Error (RMSE) of atomic positions, normalized by  $(V/N)^{1/3}$ , where  $V$  is the unit cell volume and  $N$  is the number of atoms.

**De Novo Generation.** A generated crystal is considered structurally valid if all pairwise interatomic distances exceed 0.5 Å and the unit-cell volume is at least 0.1. Compositional validity is evaluated with `SMACT` (Davies et al., 2019) by checking whether the composition admits a charge-neutral assignment of oxidation states with the Pauling electronegativity test. Unary crystals and all-metal alloys are treated as compositionally valid. To assess distributional fidelity, we compute Wasserstein distances between generated and test data distributions for atomic density  $d_\rho$ , where density is defined as  $N/V$ , and elemental composition  $d_{\text{elem}}$ , defined as the number of unique elements per unit cell.

**Thermodynamic stability.** We assess thermodynamic stability using the energy above hull ( $E_{\text{hull}}$ ). Thermodynamic stability is evaluated only for valid, non-unary generated crystals. For each such crystal, we first perform structural relaxation using `CHGNet` (Deng et al., 2023) and then compute  $E_{\text{hull}}$  with respect to the Materials Project convex hull, using the `Matbench` formation energy reference. We classify structures as *stable* if  $E_{\text{hull}} \leq 0.0$  eV/atom and as *metastable* if  $E_{\text{hull}} \leq 0.1$  eV/atom. Stability and metastability rates are computed as the fraction of valid generated crystals that are classified as stable or metastable, respectively.

**S.U.N. and MS.U.N. rates.** We report the Stability–Uniqueness–Novelty (S.U.N.) and Metastability–Uniqueness–Novelty (MS.U.N.) rates to quantify the fraction of useful generated crystals. A generated crystal is counted toward S.U.N. if it is (i) valid and non-unary, (ii) stable, (iii) unique among generated samples, and (iv) novel with respect to the training set; MS.U.N. replaces (ii) with the metastable criterion. Uniqueness is enforced by deduplicating generated crystals using `StructureMatcher`. Specifically, we cluster generated structures into equivalence classes under symmetry-aware matching and count only one representative per class. Novelty is determined by comparing each generated crystal to the training set using `StructureMatcher`. In addition, for S.U.N. and MS.U.N. calculations, we only consider generated crystals whose `CHGNet`-based structural relaxations successfully converged. A crystal is considered novel if it does not match any training structure. S.U.N. and MS.U.N. are reported as the fraction of valid generated samples that satisfy all conditions.

Table 11. **Template-conditioned crystal structure prediction on MP-20 and MPTS-52.** Evaluation under structural templates extracted from the target structure. For MCFlow, MR and RMSE are computed on generated samples matching the target template.

Model	MP-20		MPTS-52	
	MR (%) $\uparrow$	RMSE $\downarrow$	MR (%) $\uparrow$	RMSE $\downarrow$
DiffCSP++	80.27	0.0295	46.29	0.0896
SGFM	82.74	0.0288	51.79	0.0827
MCFlow-S	79.21	0.0238	73.91	0.0415
MCFlow-B	85.31	0.0210	<b>77.61</b>	<b>0.0361</b>
MCFlow-L	<b>85.96</b>	<b>0.0201</b>	74.63	0.0386

Table 12. **De novo generation results on the MPTS-52 benchmark.** Structural and compositional validity of generated crystals evaluated on MPTS-52. The MPTS-52 dataset contains 100.00% structurally valid and 88.24% compositionally valid structures. **Bold** and underline indicate the best and second-best results, respectively.

Model	Structural Validity (%) $\uparrow$	Compositional Validity (%) $\uparrow$
DiffCSP	67.47	55.80
SymmCD	87.11	78.18
DiffCSP++	<b>99.87</b>	77.52
SGEquiDiff	97.79	79.83
MCFlow-S	96.73	84.62
MCFlow-B	<u>98.34</u>	<b>85.57</b>
MCFlow-L	97.34	<u>85.21</u>

## H. Additional Experimental Results

### H.1. Template-Conditioned Crystal Structure Prediction.

We compare MCFlow with template-conditioned methods under the same evaluation setting. MCFlow remains competitive with DiffCSP++ and SGFM on both MP-20 and MPTS-52 (Table 11).

### H.2. De Novo Generation on MPTS-52.

As shown in Table 12, MCFlow exhibits a smaller reduction in structural and compositional validity on MPTS-52, which contains larger unit cells, compared to the all-atom baseline DiffCSP. In particular, MCFlow achieves higher compositional validity while maintaining competitive structural validity. These results suggest improved robustness to increased system size.

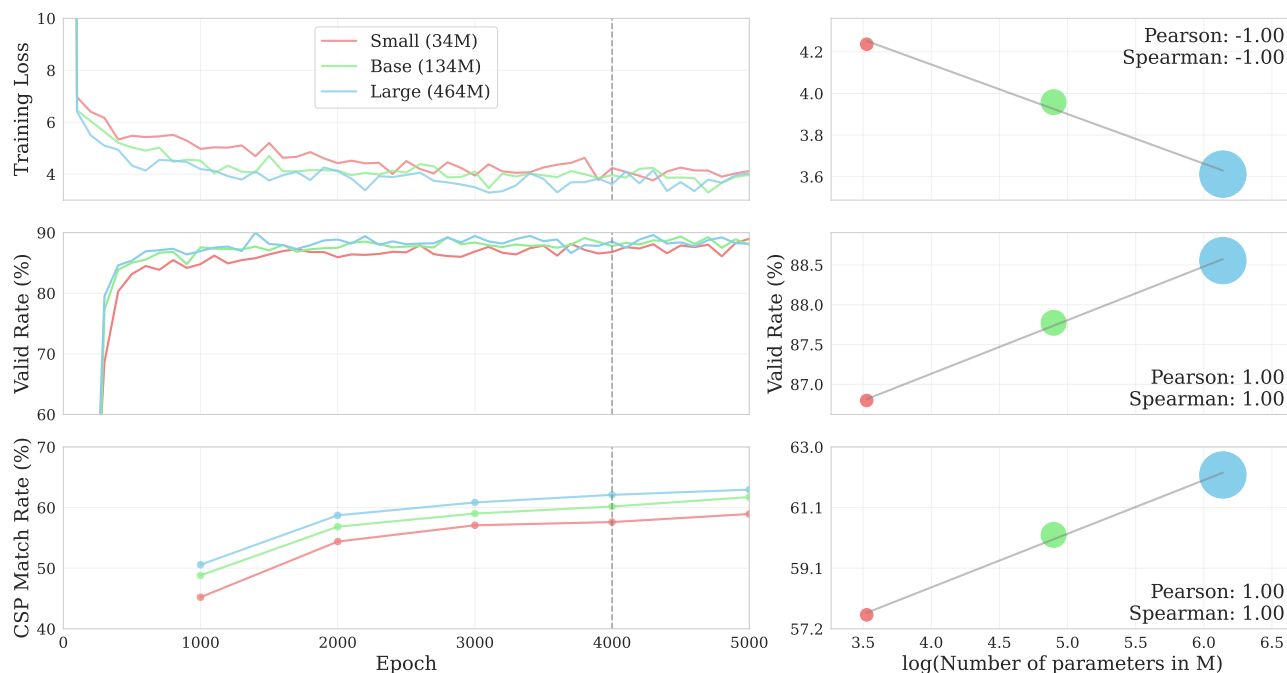


Figure 8. Scaling behavior of MCFlow across model sizes. Training loss, DNG valid rate and CSP match rate over training epochs for small, base, and large models (left). Correlation between model size and training loss, validity, and CSP match rate at epoch 4000 (right).

### H.3. Scaling Behavior Across Model Sizes.

Figure 8 summarizes the scaling behavior of MCFlow across model sizes. Larger models consistently achieve lower training loss and improved performance across both CSP and DNG, with clear monotonic trends observed in validity and CSP match rate as model capacity increases.

## I. Visualizations of Samples

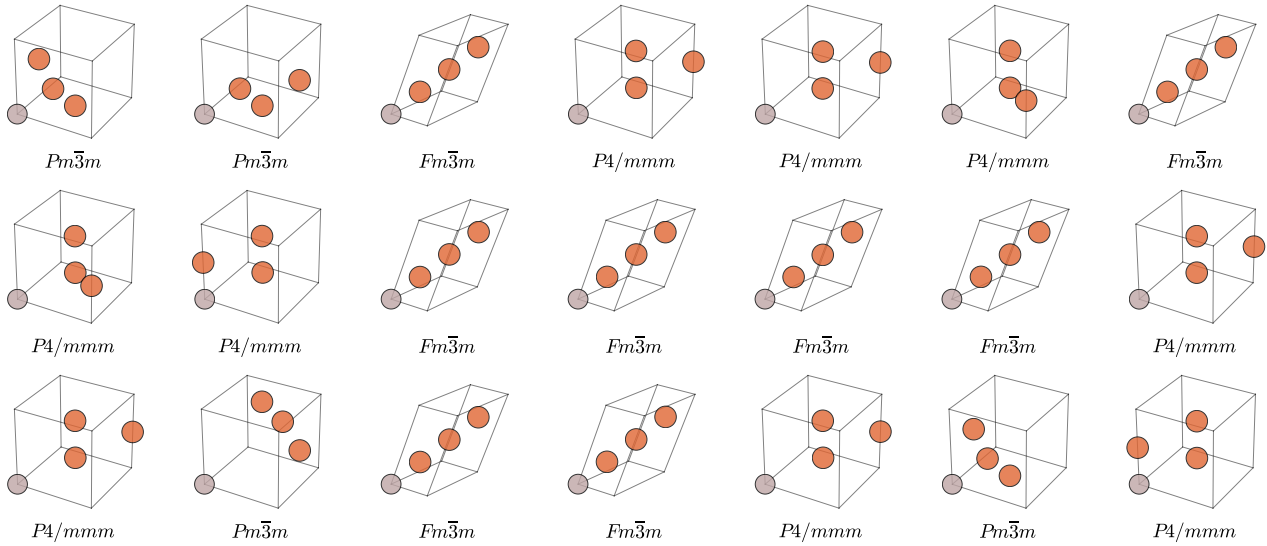


Figure 9. **Crystal structure prediction.** Given only the alloy composition  $\text{AlFe}_3$  (top-left, target crystal), MCFLOW generates diverse crystal structures with different space groups. This illustrates the model’s ability to explore multiple structures.

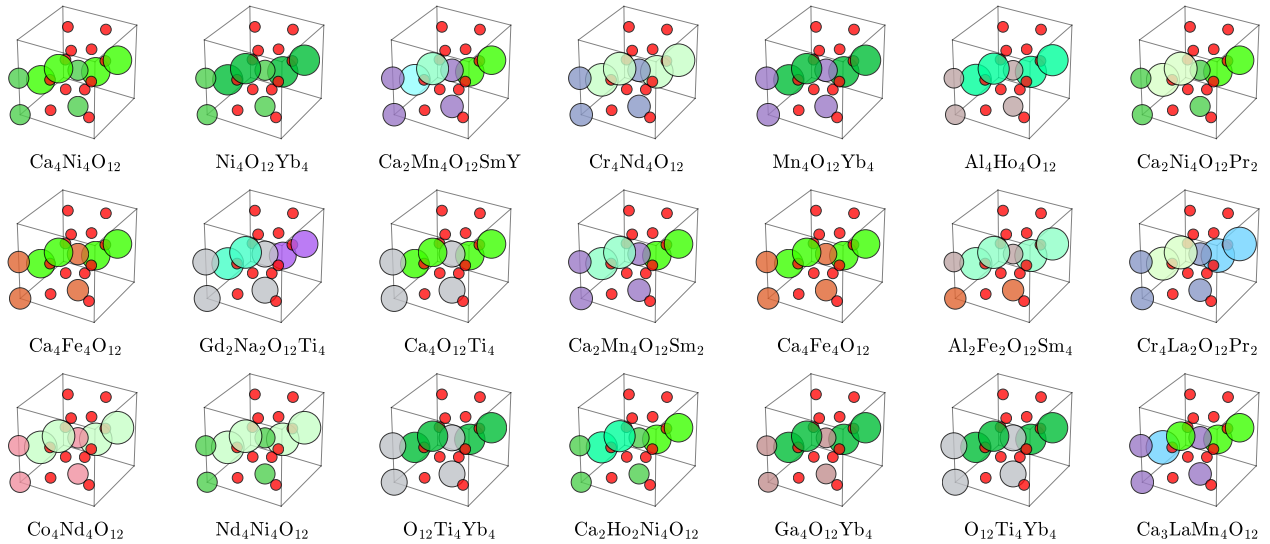


Figure 10. **Atom type generation.** Given a perovskite structure of  $\text{Ca}_4\text{Ni}_4\text{O}_{12}$  (top-left, target crystal), MCFLOW generates diverse compositions. This demonstrates the model’s ability to capture multimodal compositional distributions conditioned on a structure.

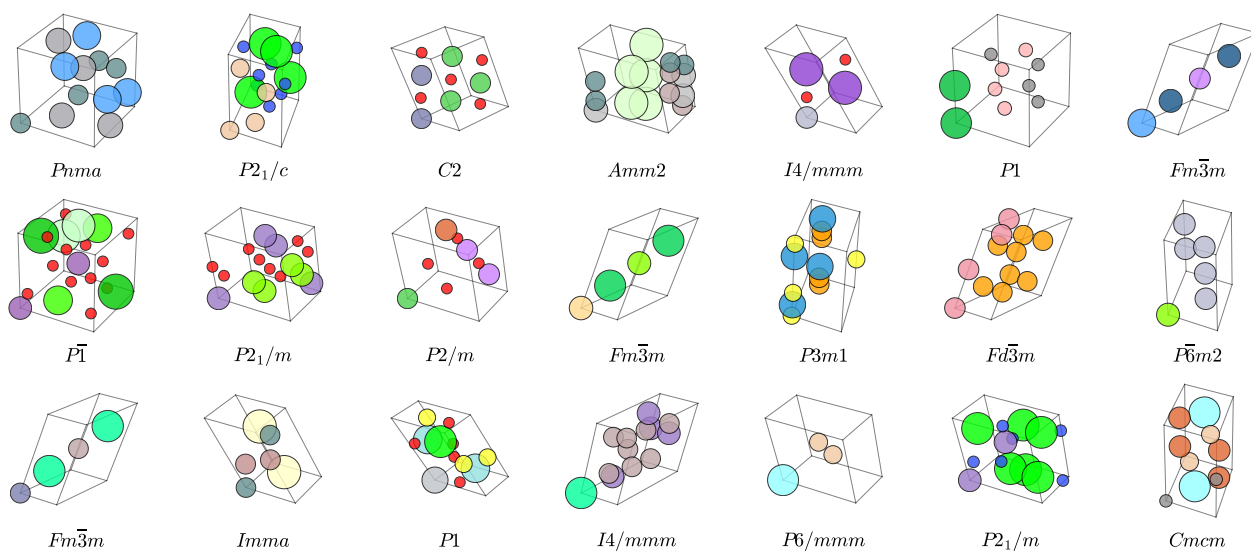


Figure 11. **De novo generation.** MCFLOW jointly generates diverse atom types and crystal structures.